

See discussions, stats, and author profiles for this publication at: <https://www.researchgate.net/publication/272362048>

# Hysteretic Gas and Vapor Sorption in Flexible Interpenetrated Lanthanide-Based Metal–Organic Frameworks with Coordinated Molecular Gating via Reversible Single-Crystal-to-Single-Cr...

ARTICLE *in* CHEMISTRY OF MATERIALS · FEBRUARY 2015

Impact Factor: 8.35 · DOI: 10.1021/cm503533r

---

CITATIONS

4

READS

77

## 7 AUTHORS, INCLUDING:



[Jon Grahame Bell](#)

Newcastle University

11 PUBLICATIONS 108 CITATIONS

[SEE PROFILE](#)



[Xiaoxia Lv](#)

Qufu Normal University

14 PUBLICATIONS 134 CITATIONS

[SEE PROFILE](#)



[Si-Fu Tang](#)

Chinese Academy of Sciences

42 PUBLICATIONS 650 CITATIONS

[SEE PROFILE](#)



[Keith Mark Thomas](#)

Newcastle University

197 PUBLICATIONS 10,082 CITATIONS

[SEE PROFILE](#)

# Hysteretic Gas and Vapor Sorption in Flexible Interpenetrated Lanthanide-Based Metal–Organic Frameworks with Coordinated Molecular Gating via Reversible Single-Crystal-to-Single-Crystal Transformation for Enhanced Selectivity

Chao Wang,<sup>†,§,||</sup> Liangjun Li,<sup>†</sup> Jon G. Bell,<sup>‡</sup> Xiaoxia Lv,<sup>§,⊥</sup> Sifu Tang,<sup>§</sup> Xuebo Zhao,<sup>\*,†,§</sup> and K. Mark Thomas<sup>\*,†</sup>

<sup>†</sup>Research Institute of Unconventional Petroleum and Renewable Energy, China University of Petroleum (East China), Qingdao 266580, P. R. China

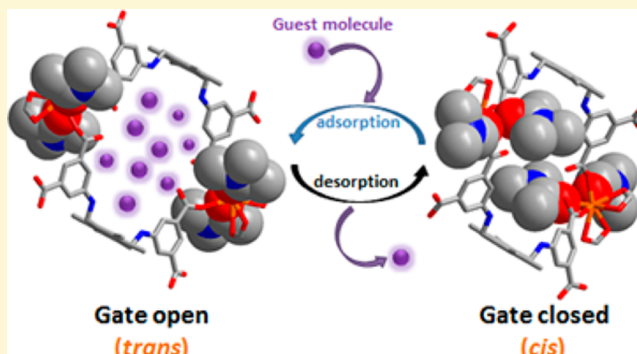
<sup>‡</sup>Wolfson Northern Carbon Reduction Laboratories, School of Chemical Engineering and Advanced Materials, Newcastle University, Newcastle upon Tyne NE1 7RU, U.K.

<sup>§</sup>Qingdao Institute of Bioenergy and Bioprocess Technology, Chinese Academy of Sciences, Qingdao, Shandong 266101, P. R. China

<sup>||</sup>University of Chinese Academy of Sciences, Beijing 100049, P. R. China

## S Supporting Information

**ABSTRACT:** A series of flexible 3-fold interpenetrated lanthanide-based metal organic frameworks (MOFs) with the formula  $[\text{Ln}(\text{HL})(\text{DMA})_2] \cdot \text{DMA} \cdot 2\text{H}_2\text{O}$ , where  $\text{Ln} = \text{La}, \text{Ce}, \text{Pr}, \text{Nd}, \text{Sm}, \text{Eu}, \text{Gd}, \text{Tb}, \text{Dy}$ , and  $\text{Er}$ , DMA = dimethylacetamide, and  $\text{H}_4\text{L} = 5,5'-(2,3,5,6-tetramethyl-1,4-phenylene)bis(methylene)bis(azanediyl)diisophthalic acid$ , have been prepared.  $[\text{Sm}(\text{HL})(\text{DMA})_2] \cdot \text{DMA} \cdot 2\text{H}_2\text{O}$  was studied as an exemplar of the series. The activated Sm(HL)(DMA)<sub>2</sub> framework exhibited reversible single-crystal-to-single-crystal (SCSC) structural transformations in response to adsorption and desorption of guest molecules. X-ray single crystal structural analysis showed that activation of  $[\text{Sm}(\text{HL})(\text{DMA})_2] \cdot \text{DMA} \cdot 2\text{H}_2\text{O}$  by heat treatment to form Sm(HL)(DMA)<sub>2</sub> involves closing of  $13.8 \times 14.8 \text{ \AA}$  channels with coordinated DMA molecules rotating into the interior of the channels with a change from *trans* to *cis* Sm coordination and unit cell volume shrinkage of  $\sim 20\%$ , to a void volume of  $3.5\%$ . Solvent exchange studies with  $\text{CH}_2\text{Cl}_2$  gave  $[\text{Sm}(\text{HL})(\text{DMA})_2] \cdot 2.8\text{CH}_2\text{Cl}_2$  which, at 173 K, had a structure similar to that of *trans*- $[\text{Sm}(\text{HL})(\text{DMA})_2] \cdot \text{DMA} \cdot 2\text{H}_2\text{O}$ .  $\text{CH}_2\text{Cl}_2$  vapor sorption on activated *cis*- $[\text{Sm}(\text{HL})(\text{DMA})_2]$  results in gate opening, and the fully loaded structure has a similar pore volume to that of *trans*- $[\text{Sm}(\text{HL})(\text{DMA})_2] \cdot 2.8\text{CH}_2\text{Cl}_2$  structure at 173 K. Solvent exchange and heat treatment studies also provided evidence for intermediate framework structural phases. Structural, thermodynamic, and kinetic aspects of the molecular gating mechanism were studied. The dynamic and structural response of the endothermic gate opening process is driven by the enthalpy of adsorption, entropic effects, and Fickian diffusion along the pores produced during framework structure development thus relating the structure and function of the material. Exceptionally high  $\text{CO}_2$  selectivity was observed at elevated pressure compared with  $\text{CH}_4$ ,  $\text{H}_2$ ,  $\text{O}_2$ , and  $\text{N}_2$  due to molecular gate opening of *cis*- $[\text{Sm}(\text{HL})(\text{DMA})_2]$  for  $\text{CO}_2$  but not for the other gases. The  $\text{CO}_2$  adsorption induced the structural transformation of *cis*- $[\text{Sm}(\text{HL})(\text{DMA})_2]$  to *trans*- $[\text{Sm}(\text{HL})(\text{DMA})_2]$ , and hysteretic desorption behavior allows capture at high pressure, with storage at lower pressure.



## 1. INTRODUCTION

Metal–organic frameworks (MOFs)<sup>1–4</sup> are a subclass of porous coordination polymers, which have shown great potential for applications in gas storage,<sup>5–7</sup> gas separation,<sup>8–10</sup> sequestration,<sup>9,11,12</sup> luminescence,<sup>13,14</sup> catalysis,<sup>15,16</sup> magnetism,<sup>17</sup> and biomedicine.<sup>18,19</sup> MOFs have extensive structural variability due to the availability of a wide range of both the organic and inorganic components, which can be used in various approaches including appropriate structure-predicting

design,<sup>20–22</sup> organic group functionalization,<sup>23–26</sup> and postsynthesis modification.<sup>27,28</sup> In addition to the structural variability, framework flexibility is also a distinguishing characteristic compared with other porous materials,<sup>29</sup> which is derived not only from the organic linker but also from variable coordination

Received: September 25, 2014

Revised: January 24, 2015

Published: February 8, 2015



geometry. The flexibility of MOFs can be observed as single-crystal-to-single-crystal (SCSC) transformations in response to guest removal and reintroduction without losing their structural integrity.<sup>30</sup> These interesting structural transformations of MOFs involve bonds forming and breaking,<sup>31</sup> dimensionality increasing and decreasing,<sup>32</sup> unit cell volume expansion and contraction,<sup>33</sup> layers slipping,<sup>34</sup> and interpenetrated networks shifting,<sup>35</sup> accompanied by a change of porosity. In contrast, structural flexibility often gives rise to the loss of framework long-range order during the activation procedure of “as-synthesized” MOFs, which involves the removal of disordered guest molecules in the framework. Several strategies have been developed to preserve the permanent porosity in MOFs, such as supercritical carbon dioxide activation<sup>36</sup> and freeze-drying methods.<sup>37</sup>

Structural interpenetration may occur in the crystal growth process and may stabilize the framework, while frequently involving the degradation or even disappearance of porosity. Despite being unpredictable, intriguingly, some reports showed that the occurrence and shifting degree of interpenetration in MOFs can be artificially controlled by modulating the synthesis methodology.<sup>38–41</sup> In this sense, interpenetration in flexible MOFs can be a reasonable approach for meeting the systematic stability requirement in response to the removal of guest molecules. In addition to these novel discoveries, in some cases, interpenetration can also enhance gas selectivity by better overlap of the attractive potential fields or adsorption induced structural transformation during the sorption process.<sup>42,43</sup>

The introduction of flexibility into metal–organic frameworks is also a potentially effective method for enhancing gas selectivity by making use of both the adaptable framework and specific interactions with guests.<sup>29,38,44–46</sup> In recent years, a number of flexible interpenetrated MOFs have presented favorable gas separation capacity, involving gas-induced structural transformation mechanisms, such as breathing and gate-opening effects.<sup>38,47–50</sup> These structural transformation phenomena can be observed both at low/high pressure and at low/ambient temperature, usually along with a stepwise and/or hysteretic sorption<sup>34,38,45–47,51,52</sup> to enhance the selectivity of a certain gas over others.<sup>31,42,53,54</sup> Although molecular simulation methods have been widely adopted to fill the gaps left by poor crystal data,<sup>55,56</sup> there are still only few reports providing details of specific structural transformations during the gas sorption process. Thus, it is desirable and challenging to build precise relationships between the structural transformations and sorption behaviors to link structure and function.

Lanthanides have large coordination spheres and variable coordination geometries. When coupled with flexible ligands, lanthanides provide the possibility for the synthesis of MOFs with both flexible frameworks and coordination geometries, potentially giving both structural and chemical diversity. A wide range of MOFs have been made with rigid tetracarboxylate linker ligands, for example, the isostructural NOTT 100-109 series, which have unsaturated copper centers when activated.<sup>57,58</sup> A new long tetracarboxylate ligand, H<sub>4</sub>L (= 5,5'-(2,3,5,6-tetramethyl-1,4-phenylene)-bis(methylene)-bis(azanediyl) diisophthalic acid), which has rotational freedom around the –CH<sub>2</sub>–NH– bonds between aromatic groups providing flexibility has been synthesized (Scheme S1, Supporting Information) and used to prepare a series of isostructural flexible 3-fold interpenetrated lanthanide-based MOFs ([Ln(HL)(DMA)<sub>2</sub>]·DMA·2H<sub>2</sub>O) with three-dimensional networks and one-dimensional channels. The ligand

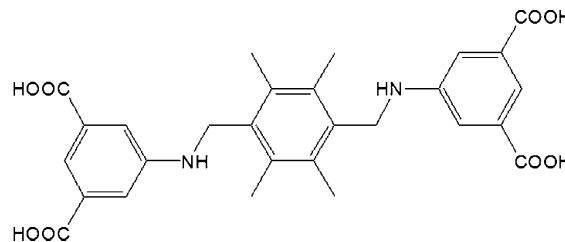
has amine groups that decorate the pore walls and may influence the adsorption and selectivity for CO<sub>2</sub>. On removal of the guest molecules, coordinated DMA molecules rotate to close the channel and act as a molecular gate. To the best of our knowledge, these MOFs are the first materials where a coordinated molecule serves as a rotational molecular gate for a pore channel. In addition to the above SCSC transformation, this material also exhibits an intermediate framework structure in responding to chloroalkane molecules (CH<sub>2</sub>Cl<sub>2</sub>, CHCl<sub>3</sub>, and C<sub>2</sub>H<sub>4</sub>Cl<sub>2</sub>) regardless of its original framework structural state “as synthesized” *trans*-[Sm(HL)(DMA)<sub>2</sub>]·DMA·2H<sub>2</sub>O or activated *cis*-[Sm(HL)(DMA)<sub>2</sub>]. Importantly, we use CO<sub>2</sub> gas as a molecular adsorption probe to perform this structural transformation process and provide thermodynamic and kinetic evidence to further understand the mechanism associated with the stepwise and hysteretic sorption. Moreover, the CH<sub>2</sub>Cl<sub>2</sub> adsorption isotherms show analogous stepwise and hysteretic sorption characteristics. X-ray diffraction results provide a detailed description of the structural transformation during the sorption process. Stepwise and hysteretic CO<sub>2</sub> adsorption characteristics contrast with the low uptakes of CH<sub>4</sub>, H<sub>2</sub>, O<sub>2</sub>, and N<sub>2</sub>, giving exceptionally high selectivity at high pressure.

## 2. EXPERIMENTAL SECTION

**2.1. Materials Used.** All reagents and solvents were commercially available, and further details are given in Supporting Information.

**2.2. Materials Synthesis.** **2.2.1. Synthesis of the Ligand.** The tetracarboxylate linker used for the synthesis of the series of MOFs is shown in Scheme 1, and the synthesis route is given in Supporting Information.

**Scheme 1.** (5,5'-(2,3,5,6-Tetramethyl-1,4-phenylene)bis(methylene)bis(azanediyl) Diisophthalic Acid (H<sub>4</sub>L)



**2.2.2. Synthesis of Diethyl 5-Aminoisophthalate.** 5-Aminoisophthalic acid (18.12 g, 0.1 mol) was dissolved in 200 mL of anhydrous ethanol, and then 20 mL of concentrated H<sub>2</sub>SO<sub>4</sub> was added to the solution. The solution was stirred under reflux for 12 h at 373 K. The pH value was adjusted to 7.0 using a 10 wt % Na<sub>2</sub>CO<sub>3</sub> aqueous solution, and this was followed by a filtration step. The organic solvent was removed from the filtrate using a rotary evaporator, and the crude product was extracted with diethyl ether. The organic layer was then dried with Na<sub>2</sub>SO<sub>4</sub>, and the solvent was removed with a rotary evaporator. The resulting product was dried under vacuum at 338 K (19.50 g, 82% yield).

**2.2.3. Synthesis of 1,4-Bis(bromomethyl)-2,3,5,6-tetramethylbenzene.** 1,2,4,5-Tetramethylbenzene (13.44 g, 0.1 mol) and paraformaldehyde (6.00 g, 0.2 mol) were added to 60 mL of HBr/HOAc (33 wt %) aqueous solution and stirred at 358 K until a white solid precipitate was observed. The solution was kept at 358 K for 20 min and was then heated to 368 K for 12 h. Then, 100 mL of deionized water was added to the above solution. The resulting product obtained after filtration was washed with deionized water and air-dried at 338 K (26.50 g, 83% yield).

**2.2.4. Synthesis of 1: Tetraethyl 5,5'-(2,3,5,6-Tetramethyl-1,4-phenylene)bis(methylene)bis(azanediyl)diisophthalate.** Diethyl 5-

aminoisophthalate (7.12 g, 30.0 mmol) was dissolved in 100 mL of acetonitrile, followed by the addition of 5.53 g (40.0 mmol) of  $K_2CO_3$ . The solution was cooled below 283 K in an ice water bath prior to the dropwise addition of 1,4-bis(bromomethyl)-2,3,5,6-tetramethylbenzene (4.80 g, 15.0 mmol, in 150 mL acetonitrile). After the addition, the solution was kept below 283 K for 1 h and stirred for 16 h at room temperature. The solvent was removed under vacuum. The crude product was extracted with  $CHCl_3$  and washed with  $H_2O$  several times. The organic layer was then dried with  $Na_2SO_4$ , and the solvent was removed with a rotary evaporator. Recrystallization of the crude solid in ethyl acetate and methanol afforded a white product. This product was dried under vacuum at 338 K (6.20 g, 65% yield).  $^1H$  NMR (600 MHz,  $CDCl_3$ )  $\delta$  (ppm): 8.05 (s, 2H), 7.50 (s, 4H), 4.40 (m, 8H), 4.34 (d, 4H), 3.76 (s, 2H), 2.32 (s, 12H), 1.41 (t, 12H). See Supporting Information, Figure S1.

**2.2.5. Synthesis of 2: 5,5'-(2,3,5,6-Tetramethyl-1,4-phenylene)-bis(methylene)bis(azanediyl) Diisophthalic Acid ( $H_4L$ ).**  $NaOH$  (2 M) (150 mL) aqueous solution was added to the solution of 1 (6.20 g, 9.80 mmol) in 200 mL of methanol/tetrahydrofuran (THF) (1:1 v/v), and the solution was stirred under reflux for 24 h at 373 K. The organic solvent was removed with a rotary evaporator at 338 K. The pH value was adjusted to 3–4 using concentrated  $HCl$ , and a pale yellow precipitate formed. The resulting solution was cooled overnight at 278 K, and the precipitate was collected by filtration, washed with water and diethyl ether, and then dried under vacuum at 338 K (4.85 g, 95% yield).  $^1H$  NMR (600 MHz,  $DMSO-d_6$ )  $\delta$  (ppm): 12.96 (b, 4H), 7.73 (s, 2H), 7.49 (d, 2H), 6.11 (s, 2H), 4.19 (s, 4H), 2.25 (s, 12H); see Figure S2 (Supporting Information). IR data (KBr,  $cm^{-1}$ ): 3409 (b), 2923 (w), 1711 (w), 1682 (m), 1606 (s), 1508 (w), 1428 (w), 1382 (w), 1297 (w), 1262 (m), 1210 (w), 1096 (w), 992 (w), 798 (w), 762 (m), 674 (m); see Figure S3 (Supporting Information).

**2.2.6. Synthesis of the Ln-MOFs.** A mixture of the organic ligand  $H_4L$  (0.10 mmol) and  $Ln(NO_3)_3 \cdot 6H_2O$  (0.20 mmol) ( $Ln = La, Ce, Pr, Nd, Sm, Eu, Gd, Tb, Dy$ , and  $Er$ ) and a mixed solvent ( $DMA/H_2O$ , 10/2 mL for the  $La^{3+}$  complex,  $DMA/H_2O$ , 6/6 mL for the  $Ce^{3+}$  and  $Pr^{3+}$  complex, and 6/6 mL with 2 drops of  $HNO_3$  for the other metal ion species) was placed in a Teflon-lined stainless steel autoclave (20 mL) and heated at 373 K for 3 days.

Characterization data for the full series of isostructural flexible 3-fold interpenetrated lanthanide-based metal organic frameworks (MOFs) with formula  $[Ln(HL)(DMA)] \cdot DMA \cdot 2H_2O$  where  $Ln = La, Ce, Pr, Nd, Sm, Eu, Gd, Tb, Dy$ , and  $Er$ ; and  $H_4L = 5,5'-(2,3,5,6-tetramethyl-1,4-phenylene)-bis(methylene)bis(azanediyl) diisophthalic acid$ , are given in Supporting Information, section 1.3.2. The data for  $trans-[Sm(HL)(DMA)] \cdot DMA \cdot 2H_2O$  are given below.

**2.2.7.  $[Sm(HL)(DMA)] \cdot DMA \cdot 2H_2O$ .** Yield: 0.039 g (42%) based on  $H_4L$ . Elemental analysis for  $C_{40}H_{58}N_5SmO_{14}$  ( $M_r = 965.26$ ) (%): calcd, H 5.85, C 49.77, N 7.26; found, H 5.51, C 48.75, N 7.12. IR data (KBr,  $cm^{-1}$ ): 3436 (b), 2917 (w), 2847 (w), 1617 (s), 1537 (s), 1432 (m), 1382 (m), 1283 (w), 1258 (w), 1147 (w), 1099 (w), 1052 (w), 1024 (w), 780 (m), 723 (w), 666 (w), 596 (w). See Figure S5 (Supporting Information).

**2.3. Characterization Methods Used.** C, H, and N analyses were carried out on an Elementar Analysensysteme Vario EL III elemental analyzer.  $^1H$  NMR spectra were recorded on a Bruker AVANCE III (600 MHz) spectrophotometer. Infrared spectra were recorded on a Thermo Fisher Nicolet 6700 FTIR Spectrometer in transmittance mode. Thermogravimetric analysis (TGA) was obtained using a Netzsch STA 449 F3 unit under a flow of nitrogen (20 mL min $^{-1}$ ) at a heating rate of 10 K min $^{-1}$  under a nitrogen atmosphere in the temperature range 303–1073 K. SEM micrographs were taken using a Hitachi S-4800 scanning electron microscope with an accelerating voltage of 3 kV.

**2.3.1. Powder X-ray Diffraction (PXRD).** Measurements were carried out using a Bruker axs D8 Advance  $\theta/2\theta$  diffractometer equipped with  $CuK_\alpha$  ( $\lambda = 1.5418 \text{ \AA}$ ), with a scan speed of 2° min $^{-1}$  and a step size of 0.02° in  $2\theta$  at room temperature. The variable temperature experiments were performed using a PANalytical X'Pert PRO MRD diffractometer with  $CuK_\alpha$  radiation ( $\lambda = 1.5418 \text{ \AA}$ ) fitted with an Anton Parr HTK1200 oven between 303 and 573 K under

static air. The powder patterns were recorded with a PIXcel3D detector in the range 5–20° ( $2\theta$ ) with a scan speed of 2° min $^{-1}$  and a step size of 0.02° in  $2\theta$ . The temperature ramp between two profiles was 10 K min $^{-1}$ , and the holding time for each temperature was 5 min before the profiles were recorded.

**2.3.2. Single Crystal X-ray Diffraction.** Single crystal X-ray diffraction data were collected on a Bruker Smart CCD diffractometer using a  $\omega$ -scan method with graphite monochromated  $MoK_\alpha$  radiation ( $\lambda = 0.71073 \text{ \AA}$ ) at 293 K. Absorption corrections were collected using a multiscan technique. The structures were solved by direct methods and developed by difference Fourier techniques using the SHELXTL software package.

**2.3.3. Crystal data.** **2.3.3.1.  $trans-[Sm(HL)(DMA)] \cdot DMA \cdot 2H_2O$ .**  $C_{36}H_{43}N_4O_{10}Sm$ ,  $M = 842.09 \text{ g mol}^{-1}$ , monoclinic, space group  $C2/c$ ,  $a = 32.84(3)$  Å,  $b = 8.998(8)$  Å,  $c = 34.21(3)$  Å,  $T = 293 \text{ K}$ ,  $V = 9119(14)$  Å $^3$ ,  $\beta = 115.564(11)^\circ$ ,  $Z = 8$ , total reflections = 22613, independent reflections = 7876,  $GOF = 1.049$ ,  $R_1[F_0 > 2\sigma(F_0)] = 0.0639$ ,  $wR_2 = 0.1432$  for all data (see Table S2, Supporting Information).

**2.3.3.2.  $cis-[Sm(HL)(DMA)]$ .**  $C_{36}H_{43}N_4O_{10}Sm$ ,  $M = 842.09 \text{ g mol}^{-1}$ , monoclinic, space group  $C2/c$ ,  $a = 32.14(2)$  Å,  $b = 9.156(6)$  Å,  $c = 26.864(18)$  Å,  $\beta = 112.859(7)^\circ$ ,  $T = 293 \text{ K}$ ,  $V = 7285(8)$  Å $^3$ ,  $Z = 8$ , total reflections = 21958, independent reflections = 6376,  $GOF = 1.051$ ,  $R_1[F_0 > 2\sigma(F_0)] = 0.0625$ ,  $wR_2 = 0.1434$  for all data (see Table S2, Supporting Information).

**2.3.3.3.  $trans-[Sm(HL)(DMA)] \cdot 2.8CH_2Cl_2$  (173 K).**  $C_{36}H_{43}N_4O_{10}Sm$ ,  $M = 842.09 \text{ g mol}^{-1}$ , monoclinic, space group  $C2/c$ ,  $a = 32.599(5)$  Å,  $b = 8.8449(14)$  Å,  $c = 26.246(8)$  Å,  $\beta = 116.457(2)^\circ$ ,  $T = 173(2) \text{ K}$ ,  $V = 8840(3)$  Å $^3$ ,  $Z = 8$ , total reflections = 29796, independent reflections = 7782,  $GOF = 1.048$ ,  $R_1[F_0 > 2\sigma(F_0)] = 0.0507$ ,  $wR_2 = 0.0929$  for all data (Table S3, Supporting Information).

**2.3.3.4.  $trans-[La(HL)(DMA)] \cdot DMA \cdot 2H_2O$ .**  $C_{36}H_{43}N_4O_{10}La$ ,  $M = 830.65 \text{ g mol}^{-1}$ , monoclinic, space group  $C2/c$ ,  $a = 32.985(7)$  Å,  $b = 8.9901(18)$  Å,  $c = 34.432(7)$  Å,  $\beta = 115.591(2)^\circ$ ,  $T = 293 \text{ K}$ ,  $V = 9209(3)$  Å $^3$ ,  $Z = 8$ , total reflections = 25159, independent reflections = 8103,  $GOF = 1.127$ ,  $R_1[F_0 > 2\sigma(F_0)] = 0.0554$ ,  $wR_2 = 0.1480$  for all data (see Table S4, Supporting Information).

**2.4. Adsorption Measurements.** **2.4.1. Isotherm Studies.** Gas sorption isotherms were measured using an Intelligent Gravimetric Analyzer (IGA-001, Hiden Isochema, Warrington, UK). The system is an ultrahigh vacuum (UHV) system comprising a fully computer controlled microbalance with both pressure and temperature regulation systems. The microbalance had a long-term stability of  $\pm 1 \mu\text{g}$  with a weighing resolution of 0.2  $\mu\text{g}$ . The pressure transducers had ranges of 0–0.1 and 0–2 MPa. Carbon dioxide sorption at 195 K was carried out using a solid carbon dioxide–acetone bath. Gas sorption isotherms between 273 and 333 K were obtained using a circulating water–ethylene glycol bath controlled by a computer using IGA software. The  $CH_2Cl_2$  used to generate the vapor for the isotherm measurements was degassed fully by repeated evacuation and vapor equilibration cycles of the liquid supply side of the vapor reservoir. The gas or vapor pressure was gradually increased to the desired value over a time-scale of ~30 s to prevent disruption of the microbalance. Therefore, the period over which the pressure change occurred was very small compared with the adsorption kinetics allowing isotherm adsorption kinetics to be measured for each pressure step. The sample temperature was measured using a thermocouple located 5 mm from the sample. The sample was outgassed to constant weight at  $< 10^{-6}$  Pa and 393 K prior to commencing adsorption measurements. Surface excess adsorption isotherms were determined for high pressure  $CO_2$  adsorption using the buoyancy correction based on the crystallographic density for the desolvated framework material.

Saturated vapor pressures were calculated using the Antoine equation:

$$\log p_0 = A - \frac{B}{T + C} \quad (1)$$

where  $p_0$  is the saturated vapor pressure (Torr),  $T$  is the temperature (°C), and  $A$ ,  $B$ , and  $C$  are adsorbate dependent constants. The parameters used for each adsorptive are as follows:  $CH_2Cl_2$  (233–313

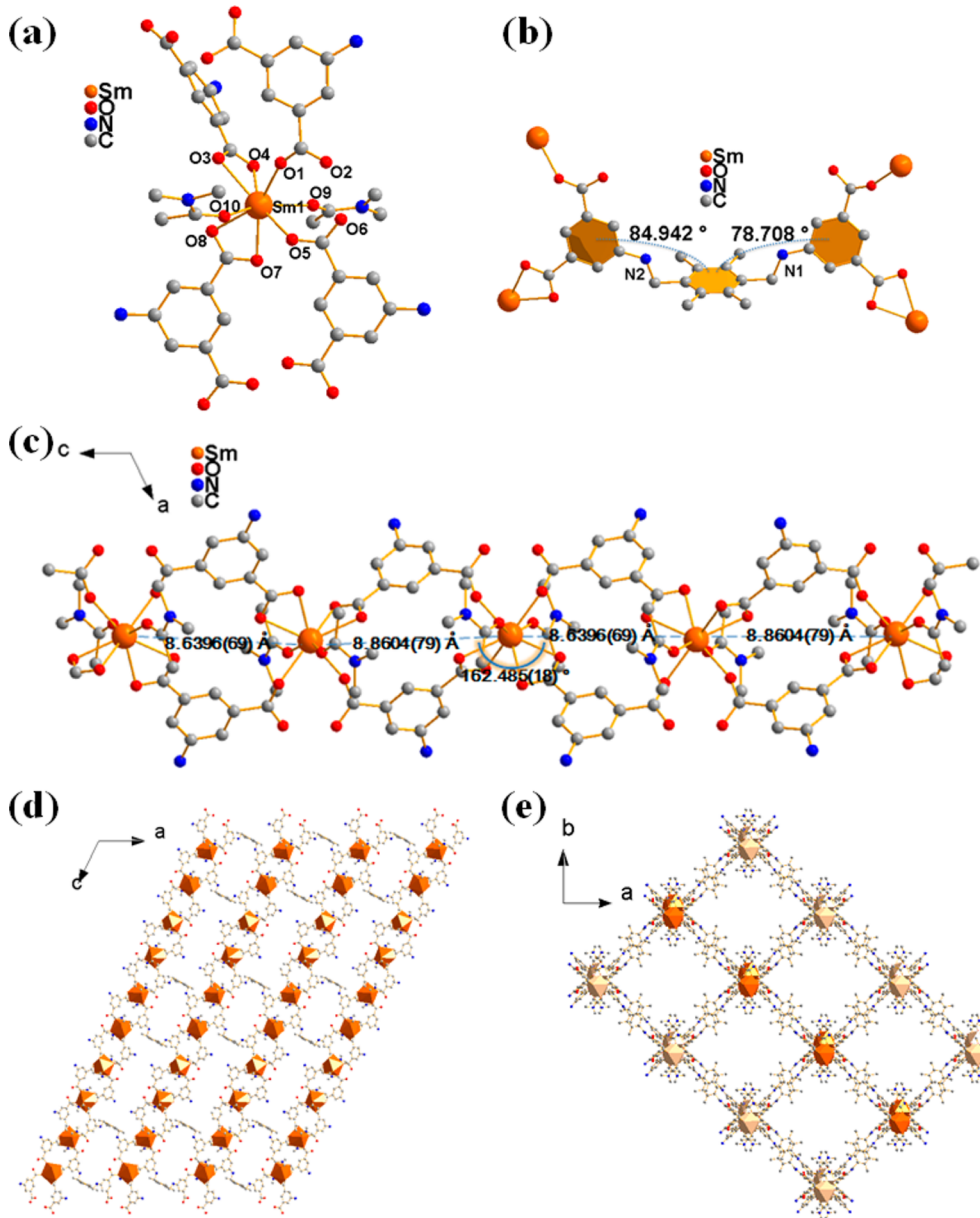


**Figure 1.** X-ray crystal structures of a single network of  $[\text{Sm}(\text{HL})(\text{DMA})_2]\cdot\text{DMA}\cdot2\text{H}_2\text{O}$ . The coordination environments of (a) the  $\text{Sm}^{3+}$  node and (b) ligand  $\text{HL}^{3-}$ . (c) The metal chain linked by ligands  $\text{HL}^{3-}$  along the  $b$ -axis. (d) The two-dimensional layer network formed by the metal chains and ligands  $\text{HL}^{3-}$  viewed along the  $b$ -axis. (e) The three-dimensional framework viewed along the  $c$ -axis. (Sm, orange; O, red; N, blue; and C, gray; H atoms and guest molecules are omitted for clarity.)

K) (A) 7.4092, (B) 1325.9, (C) 252.6; carbon dioxide (77–303 K) (A) 7.81024, (B) 995.705, (C) 293.475.<sup>59</sup>

**2.4.2. Temperature Swing Experiments.** Kinetic studies of the framework transformation of *cis*- $[\text{Sm}(\text{HL})(\text{DMA})_2]$  to *trans*- $[\text{Sm}(\text{HL})(\text{DMA})_2]$  were studied. The sample was allowed to equilibrate, and the amount of  $\text{CO}_2$  adsorbed on the sample was  $0.6 \text{ mmol g}^{-1}$  at equilibrium. Meanwhile, the circulation bath was set to the desired temperature (313, 303, 293, or 273 K). The liquid circulation bath system was equilibrated using a plug to block the liquid overflow. After the sample reached equilibrium, the heater was removed quickly and replaced by the water bath. This operation took  $\sim 30$  s, and the desired sample temperatures (293–313 K) were reached within 60–90 s. This time scale was very short, compared to the kinetic equilibration times for the framework transformation. The cooling to 273 K took longer, while the adsorption kinetics were much faster and followed the qualitative trend with temperature. However, the kinetics parameters were not quantifiable because of the relatively slow thermal equilibration.

### 3. RESULTS AND DISCUSSION

**3.1. Structure Characterization.** The experimental and simulated PXRD patterns of *trans*- $[\text{Ln}(\text{HL})(\text{DMA})_2]\cdot\text{DMA}\cdot2\text{H}_2\text{O}$  ( $\text{Ln} = \text{La}, \text{Ce}, \text{Pr}, \text{Nd}, \text{Sm}, \text{Eu}, \text{Gd}, \text{Tb}, \text{Dy}, \text{Er}$ ) are shown in Supporting Information (Figures S6a and b). The peak positions for all of the materials are in good agreement indicating that all of the *trans*- $[\text{Ln}(\text{HL})(\text{DMA})_2]\cdot\text{DMA}\cdot2\text{H}_2\text{O}$  MOFs are isostructural. Single-crystal X-ray diffraction results reveal that *trans*- $[\text{Ln}(\text{HL})(\text{DMA})_2]\cdot\text{DMA}\cdot2\text{H}_2\text{O}$  crystallize in the monoclinic space group  $C2/c$  for  $\text{Ln} = \text{Sm}, \text{La}$ , and  $\text{Tb}$  (Table S1, Supporting Information). *trans*- $[\text{Sm}(\text{HL})(\text{DMA})_2]\cdot\text{DMA}\cdot2\text{H}_2\text{O}$  was selected as a representative example of the series for detailed crystal structure analysis and adsorption studies.

The solvothermal reaction of  $\text{H}_4\text{L}$  with  $\text{Sm}(\text{NO}_3)_3\cdot6\text{H}_2\text{O}$  in an acidic ( $\text{HNO}_3$ ) mixture of  $\text{H}_2\text{O}/\text{DMA}$  ( $v/v = 1/1$ ) at 373 K

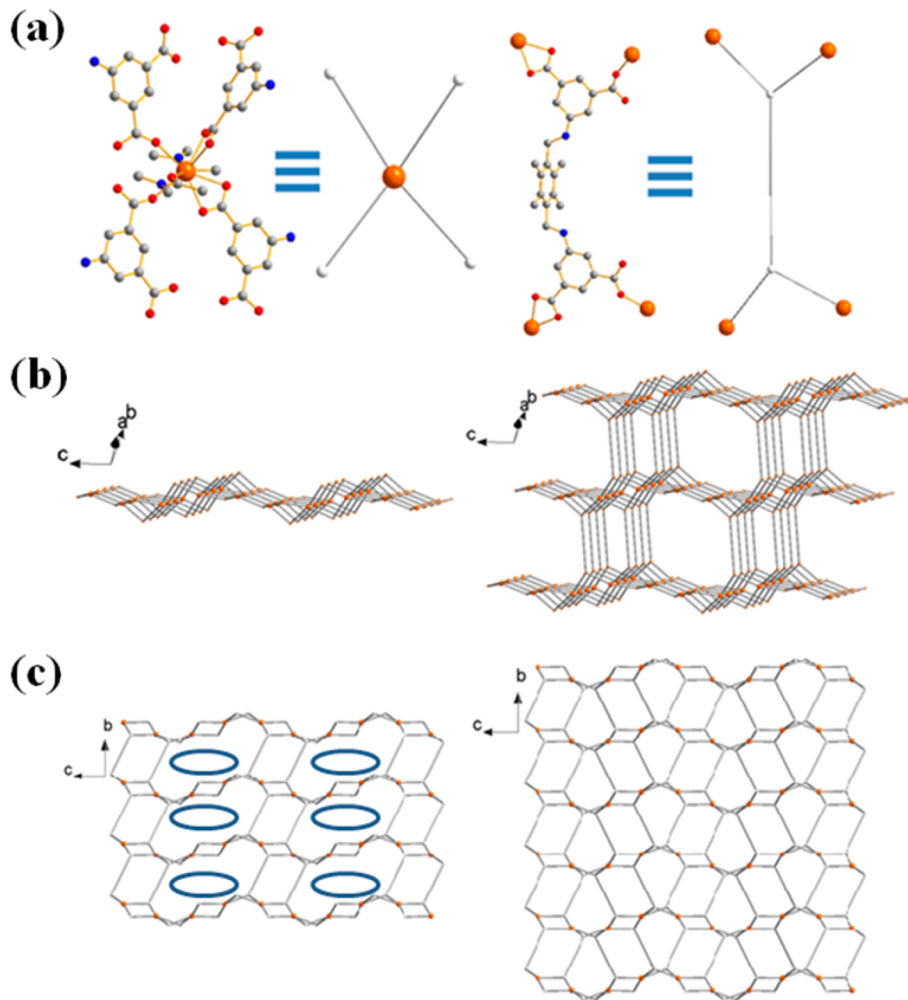


**Figure 2.** Simplified views of a single network of  $[\text{Sm}(\text{HL})(\text{DMA})_2]\cdot\text{DMA}\cdot 2\text{H}_2\text{O}$ . (a) The four-connected  $\text{Sm}^{3+}$  node and  $\text{HL}^{3-}$  node. (b) The single 2D layer and 3D network. (c) The layer and network along the *a*-axis.

for 3 days afforded the colorless, needle-shaped crystals of solvated framework  $[\text{Sm}(\text{HL})(\text{DMA})_2]\cdot\text{DMA}\cdot 2\text{H}_2\text{O}$ . The single-crystal X-ray structure of  $[\text{Sm}(\text{HL})(\text{DMA})_2]\cdot\text{DMA}\cdot 2\text{H}_2\text{O}$  shows an infinite three-dimensional (3D) (4,4)-connected framework constructed from mononuclear  $\text{Sm}^{3+}$  nodes each linked to four others by four ligands  $\text{HL}^{3-}$  (Figure 1). The framework structure is 3-fold interpenetrated and consists of three identical crystallographically independent networks.

As illustrated in Figure 1a, each  $\text{Sm}^{3+}$  exhibits 8-coordination through two bidentate carboxylate groups, two monodentate carboxylate groups, and a pair of DMA molecules to form a 4-connected node (see Figure S11, Supporting Information). Each ligand  $\text{HL}^{3-}$  binds to four separate  $\text{Sm}^{3+}$  centers and acts as a 4-connected linker (Figure 1b). Additionally, the middle phenyl ring of ligand  $\text{HL}^{3-}$  is significantly tilted toward end phenyl rings with dihedral angles of  $78.71^\circ$  and  $84.94^\circ$ , respectively. It is apparent that the middle aromatic ring in the linker is perpendicular to the plane consisting of the terminal aromatic groups.

Each single network consists of infinite 2D layers. For a single layer, the ligand  $\text{HL}^{3-}$  bridges two  $\text{Sm}^{3+}$  through its adjacent carboxylate groups and forms infinite helical chains along the *c*-axis. The Sm atoms are almost coplanar with  $\text{Sm}-\text{Sm}-\text{Sm}$  angles of  $162.485(18)^\circ$ , while the  $\text{Sm}-\text{Sm}$  distances

through the carboxylate groups alternately vary from  $8.6396(69)$  to  $8.8604(79)$  Å (Figure 1c). The metal carboxylate chains are bridged by  $\text{HL}^{3-}$  linkers to form a 2D layer network (Figure 1d), and the remaining carboxylic binding sites of  $\text{HL}^{3-}$  ligands extend downward and upward to link the adjacent layers, leading to the formation of a 3D framework (Figure 1e). From the viewpoint of network topology, the structure is a rare binodal (4,4)-connected *umc* network.

To understand the construction of the resultant 3D 3-fold interpenetrated framework of  $[\text{Sm}(\text{HL})(\text{DMA})_2]\cdot\text{DMA}\cdot 2\text{H}_2\text{O}$ , it is necessary to simplify the chemical composition of the networks. The individual 3D motif can be reduced as a (4,4)-connected network if the ligand  $\text{HL}^{3-}$  is defined as a four-connected node linking to four  $\text{Sm}^{3+}$ , and the  $\text{Sm}^{3+}$  is viewed as a four-connected node (Figure 2a). A single layer shows two types of micropores viewed along the *a*-axis. However, the layer is further connected by ligands  $\text{HL}^{3-}$  to generate a 3D framework (Figure 2b), and the bigger voids (marked in Figure 2c) are divided into small ones. Similarly, the geometric construction transformation along the *b*-axis is observed (Figure S7a, Supporting Information). Furthermore, the three-dimensional framework consisting of 2D layers and  $\text{HL}^{3-}$  linkers exhibits square channels along the *c*-axis (Figures 1e and S7b, Supporting Information).

The three independent networks are shown in red, blue, and yellow. The geometrical configurations of these three networks are identical, and they are related to each other by a translational vector of 9.00 Å along the *b*-axis. Simplified views of the 3-fold interpenetrated framework structure are shown in Figure S8 (Supporting Information).

Because of the interpenetration in [Sm(HL)(DMA)<sub>2</sub>]·DMA·2H<sub>2</sub>O, the channels in a single 3D network are mainly filled by the other two 3D networks (Figure 3). These three

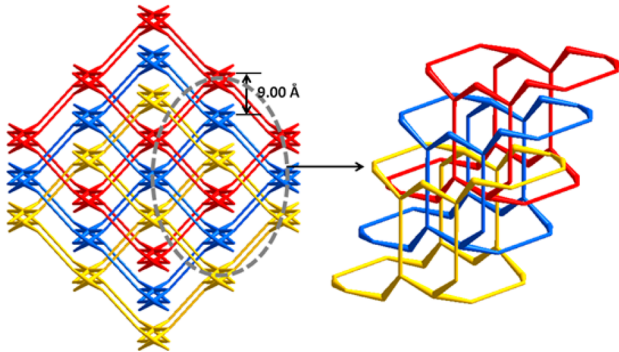


**Figure 3.** Simplified view of the 3-fold interpenetration framework of [Sm(HL)(DMA)<sub>2</sub>]·DMA·2H<sub>2</sub>O.

interpenetrated networks are related by a single translational vector with the shortest interpenetration vector [0,1,0] of 9.00 Å. Interestingly, even after 3-fold interpenetration [Sm(HL)(DMA)<sub>2</sub>]·DMA·2H<sub>2</sub>O still possesses some void space along the *b*-axis (Figure 4a). The resulting 3-fold interpenetration framework exhibits 13.8 × 14.8 Å channels along the *b*-axis (Figure 4).

The structure of [La(HL)(DMA)<sub>2</sub>]·DMA·2H<sub>2</sub>O is very similar to that of [Sm(HL)(DMA)<sub>2</sub>]·DMA·2H<sub>2</sub>O with virtually identical coordination geometries (Figure S11, Supporting Information). The dihedral angles between the center aromatic and terminal aromatic rings were 78.75° and 84.97° for [La(HL)(DMA)<sub>2</sub>]·DMA·2H<sub>2</sub>O, and 78.71° and 84.94° for [Sm(HL)(DMA)<sub>2</sub>]·DMA·2H<sub>2</sub>O. The corresponding dihedral angles for [Sm(HL)(DMA)<sub>2</sub>]·2.8CH<sub>2</sub>Cl<sub>2</sub> (173 K) were 78.69° and 89.85°, respectively, and this shows a small amount of

conformational flexibility. The PLATON<sup>60</sup> pore volumes were 0.217 cm<sup>3</sup> g<sup>-1</sup> (26.0%), 0.21 cm<sup>3</sup> g<sup>-1</sup> (25.9%), and 0.19 cm<sup>3</sup> g<sup>-1</sup> (24.1%) for [La(HL)(DMA)<sub>2</sub>]·DMA·2H<sub>2</sub>O, [Sm(HL)(DMA)<sub>2</sub>]·DMA·2H<sub>2</sub>O, and [Sm(HL)(DMA)<sub>2</sub>]·2.8CH<sub>2</sub>Cl<sub>2</sub> (173 K), respectively.

**3.2. Structural Transformations.** In the structural transformation from *trans*-[Sm(HL)(DMA)<sub>2</sub>]·DMA·2H<sub>2</sub>O to *cis*-[Sm(HL)(DMA)<sub>2</sub>], the channels are transformed into discontinuous voids during the desolvation process. Viewed along the *b*-axis, the channel windows are clearly blocked off by the coordinated DMA molecules in *cis*-[Sm(HL)(DMA)<sub>2</sub>]. During the desolvation process, the shortest interpenetration vector of the 3-fold interpenetration frameworks elongates from 9.00 to 9.16 Å along the *b*-axis. Viewed along the same direction, for a single network, the approximate diameter of the channel window varies from 24.2 × 14.0 to 14.6 × 14.6 Å, coupled with the intersection angle varying from 95.6° to 86.7°. For a detailed view, two C—N—C angles vary from 125.0(9)° (C(21)—N(2)—C(16)) and 125.3(8)° (C(6)—N(1)—C(9)) in *trans*-[Sm(HL)(DMA)<sub>2</sub>]·DMA·2H<sub>2</sub>O to 119.6(8)° (C(21)—N(2)—C(20)) and 124.9(8)° (C(6)—N(1)—C(9)) in *cis*-[Sm(HL)(DMA)<sub>2</sub>]. The Sm—O bond lengths for DMA and bidentate and monodentate carboxylate coordination were similar in *cis*-[Sm(HL)(DMA)<sub>2</sub>] and *trans*-[Sm(HL)(DMA)<sub>2</sub>]·DMA·2H<sub>2</sub>O.

The coordination geometries of Sm<sup>3+</sup> centers change markedly and one coordinated DMA molecule in the *trans*-[Sm(HL)(DMA)<sub>2</sub>]·DMA·2H<sub>2</sub>O framework rotates to the *a*-axis to close the channels along the *b*-axis in *cis*-[Sm(HL)(DMA)<sub>2</sub>] framework with the intersection angle between two Sm—O bonds changing from 151.21° in *trans*-[Sm(HL)(DMA)<sub>2</sub>]·DMA·2H<sub>2</sub>O to 76.30° in *cis*-[Sm(HL)(DMA)<sub>2</sub>]. Therefore, the structural transformation can be described as *trans*-[Sm(HL)(DMA)<sub>2</sub>]·DMA·2H<sub>2</sub>O changing to activated *cis*-[Sm(HL)(DMA)<sub>2</sub>]. Generally, the structural transformations induced by guest removal are classified into three categories: crystalline to amorphous state transformations with the framework collapsing and crystal to crystal transformations with and without the cleavage and regeneration of coordination bonds.<sup>30</sup> The structural transformation of *trans*-[Sm(HL)(DMA)<sub>2</sub>]·DMA·2H<sub>2</sub>O upon guest removal is shown in Figure 5. Simplified views of the change in interpenetration on

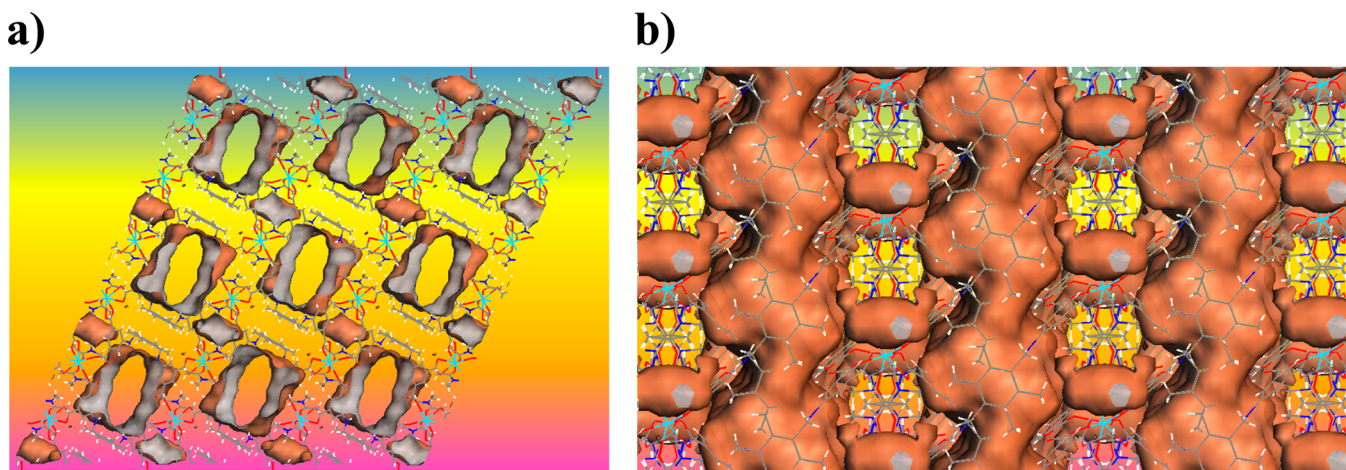


**Figure 4.** Perspective views of the framework of *trans*-[Sm(HL)(DMA)<sub>2</sub>]·DMA·2H<sub>2</sub>O. Connolly surface representation of the 3-fold interpenetration framework structure and channels (orange) of *trans*-[Sm(HL)(DMA)<sub>2</sub>]·DMA·2H<sub>2</sub>O along the (a) *b*-axis and (b) *c*-axis with a Connolly probe diameter of 2.4 Å. (Sm, light blue; O, red; N, blue; C, gray; and H, white; guest molecules are omitted for clarity.)

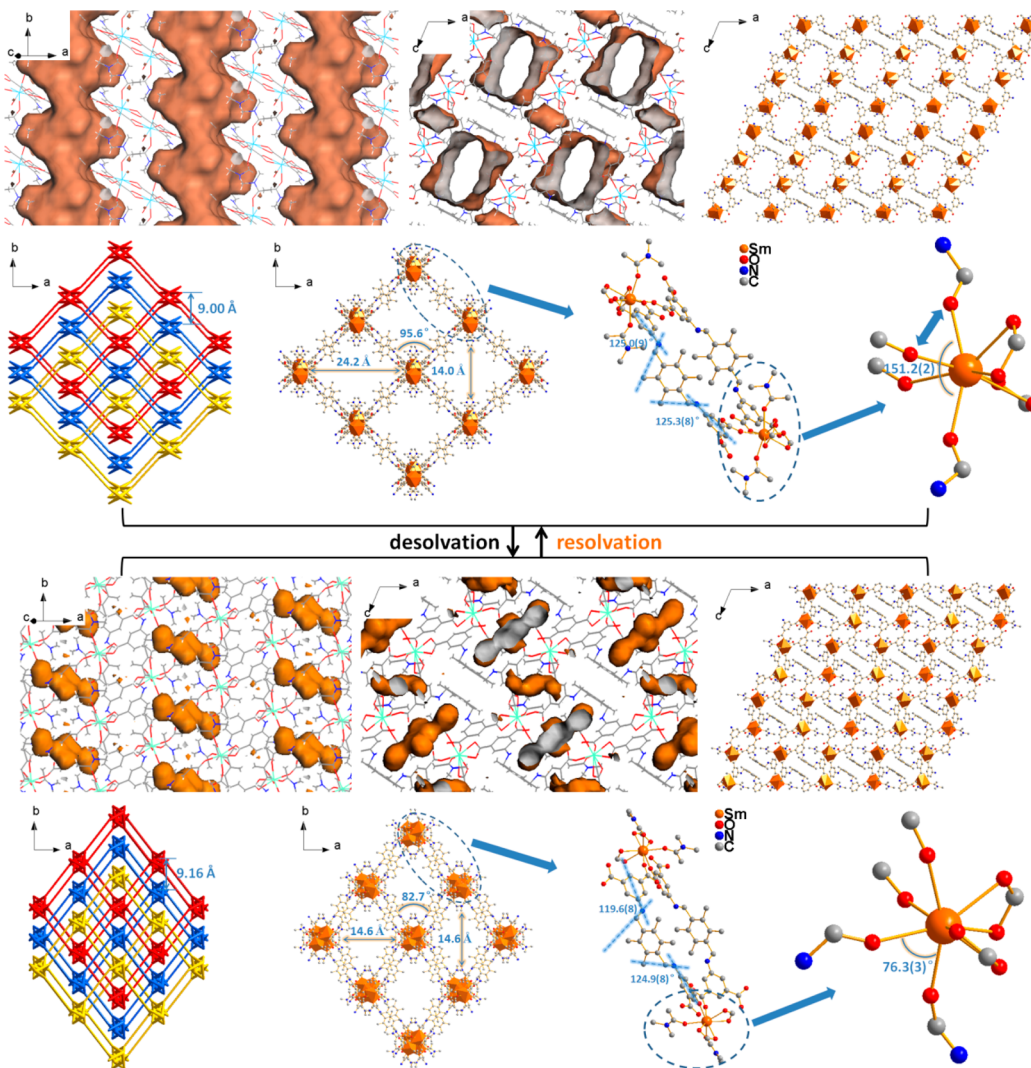


**Figure 5.** Structural transformations between *trans*-[Sm(HL)(DMA)<sub>2</sub>]·DMA·2H<sub>2</sub>O and *cis*-[Sm(HL)(DMA)<sub>2</sub>].

desolvation of *trans*-[Sm(HL)(DMA)<sub>2</sub>]·DMA·2H<sub>2</sub>O and resolvation of *cis*-[Sm(HL)(DMA)<sub>2</sub>] are shown in Figure S9 (Supporting Information). Single crystals remained physically intact after heating for 4 h at 393 K under vacuum, but a significant phase transformation took place, and a new single-crystal form *cis*-[Sm(HL)(DMA)<sub>2</sub>] was formed (Figures 4 and 5). The single-crystal structure determination of the desolvated *cis*-[Sm(HL)(DMA)<sub>2</sub>] shows that the monoclinic crystal structure and C2/c space group are maintained, while the unit cell volume shrinks by ~20% (Table S2, Supporting Information). Detailed illustrations in Figure 5 show that although no change occurs in the coordination bonds of Sm<sup>3+</sup> centers, two O atoms from a monodentate carboxylate group and a DMA molecule almost exchange the coordination positions to the Sm<sup>3+</sup> center and the distance between two adjacent Sm<sup>3+</sup> along the *a*-axis shortens markedly, which is the leading cause of the shrinkage of unit cell volume from 9119(14) to 7285(8) Å<sup>3</sup> (Figure 5).

The rotatable coordinated DMA molecule in *cis*-[Sm(HL)(DMA)<sub>2</sub>], which is almost orthogonal to the *b*-axis, points toward the interior of the channel and cuts it into discontinuous voids (Figure 5), coupled with a significant decrease of void volume to only 3.5% calculated by PLATON,<sup>60</sup> much lower than that of the *trans*-[Sm(HL)-

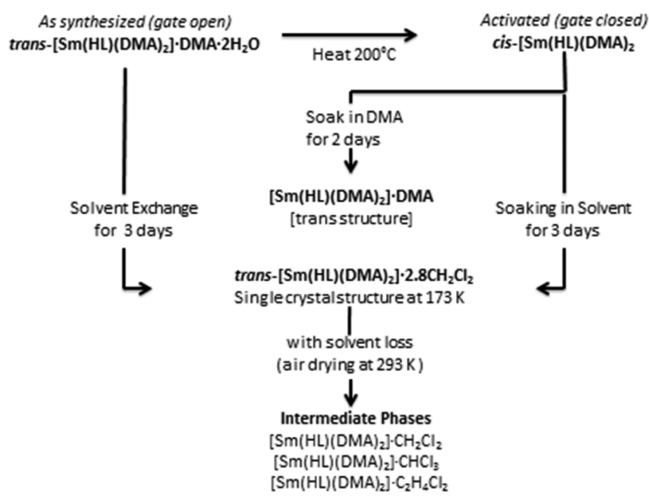
(DMA)<sub>2</sub>]·DMA·2H<sub>2</sub>O framework (25.9%). Thus, guest removal leads to the structural transformation of *trans*-[Sm(HL)(DMA)<sub>2</sub>]·DMA·2H<sub>2</sub>O, in which the framework undergoes a marked change of coordination geometry for Sm<sup>3+</sup> centers, which shrinks both the void and unit cell volumes, while maintaining the overall framework connectivity.

**3.2.1. Heat Treatment Studies.** The experimental PXRD profiles for *trans*-[Sm(HL)(DMA)<sub>2</sub>]·DMA·2H<sub>2</sub>O and *cis*-[Sm(HL)(DMA)<sub>2</sub>] were in good agreement with the corresponding simulated profiles calculated from single crystal structure data (see Figure S6a, Supporting Information). The conversion of *trans*-[Sm(HL)(DMA)<sub>2</sub>]·DMA·2H<sub>2</sub>O into the fully desolvated *cis*-[Sm(HL)(DMA)<sub>2</sub>] with heat treatment temperature (HTT) under atmospheric pressure was monitored using PXRD studies and is shown in Figures S12a and b (Supporting Information). At 433 K, close to the boiling point of DMA (439 K), strong reflections at  $2\theta = 6.5^\circ$  (intermediate phase) and  $7.4^\circ$  (*cis*-[Sm(HL)(DMA)<sub>2</sub>]) were observed with the former peak being absent at 473 K confirming complete transformation to *cis*-[Sm(HL)(DMA)<sub>2</sub>] and the coexistence of three correlative structures. The first sharp weight loss occurs at 438 K in the TGA profile of *trans*-[Sm(HL)(DMA)<sub>2</sub>]·DMA·2H<sub>2</sub>O (Figure S15, Supporting Information). The phase transformation continued until the new phase of *cis*-[Sm(HL)(DMA)<sub>2</sub>] was

completely formed at 473 K, corresponding to the end of the initial weight loss in the TGA profile. It is evident that crystallinity is maintained throughout the conversion of *trans*-[Sm(HL)(DMA)<sub>2</sub>]**·**DMA<sub>2</sub>H<sub>2</sub>O to *cis*-[Sm(HL)(DMA)<sub>2</sub>] and that the latter is stable after cooling to ambient conditions. The *trans*-[Ln(HL)(DMA)<sub>2</sub>]**·**DMA<sub>2</sub>H<sub>2</sub>O (Ln = Sm, La, Pr, Nd, Eu, Gd, Tb, Dy, and Er) series have very similar PXRD (Figure S6b, Supporting Information) and TGA (Figure S16, Supporting Information) profiles.

**3.2.2. Guest Exchange Studies.** Flexible frameworks may display intermediate structural states.<sup>34,45,61</sup> This aspect was studied by solvent exchange with *trans*-[Sm(HL)(DMA)<sub>2</sub>]**·**DMA<sub>2</sub>H<sub>2</sub>O and soaking *cis*-[Sm(HL)(DMA)<sub>2</sub>] in various solvents (see Scheme 2 and sample nomenclature in Table S5,

**Scheme 2. Framework Structural Transformations Involving Solvent Guest Exchange and Heat Treatment**



Supporting Information). The DMA (B. Pt. = 439 K) soaked *cis*-[Sm(HL)(DMA)<sub>2</sub>] sample had a PXRD profile similar to that of *trans*-[Sm(HL)(DMA)<sub>2</sub>]**·**DMA<sub>2</sub>H<sub>2</sub>O (see Figure 6). Hence, the framework *trans* to *cis* structural transformation on activation by heat treatment is reversed by soaking in DMA.

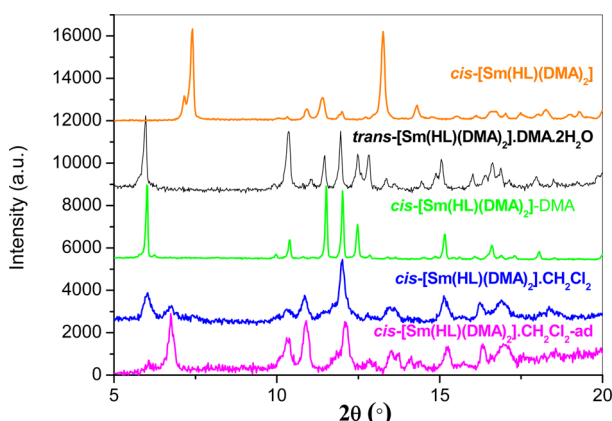


**Figure 6.** PXRD profiles for *trans*-[Sm(HL)(DMA)<sub>2</sub>]**·**DMA<sub>2</sub>H<sub>2</sub>O, *cis*-[Sm(HL)(DMA)<sub>2</sub>], DMA soaked *cis*-[Sm(HL)(DMA)<sub>2</sub>], CH<sub>2</sub>Cl<sub>2</sub> soaked *cis*-[Sm(HL)(DMA)<sub>2</sub>], and CH<sub>2</sub>Cl<sub>2</sub> soaked *cis*-[Sm(HL)(DMA)<sub>2</sub>] with air drying (ad). Intensities have been rescaled to avoid the overlap of peaks.

The single crystal structure of *trans*-[Sm(HL)(DMA)<sub>2</sub>]**·**2.8CH<sub>2</sub>Cl<sub>2</sub> at 173 K was very similar to the structure of *trans*-[Sm(HL)(DMA)<sub>2</sub>]**·**DMA<sub>2</sub>H<sub>2</sub>O (Figures S10 and S11, Supporting Information) and hence the simulated PXRD profiles are very similar (Figure S13a, Supporting Information). The PXRD profiles of solvent exchanged samples *trans*-[Sm(HL)(DMA)<sub>2</sub>]**·**CH<sub>2</sub>Cl<sub>2</sub> and *cis*-[Sm(HL)(DMA)<sub>2</sub>]**·**CH<sub>2</sub>Cl<sub>2</sub> were similar irrespective of the starting *cis* or *trans*-[Sm(HL)(DMA)<sub>2</sub>] framework structure, with relatively broad peaks indicative of lower crystallinity (see Figures 6 and S13c, Supporting Information). Drying *trans*-[Sm(HL)(DMA)<sub>2</sub>]**·**CH<sub>2</sub>Cl<sub>2</sub> and *cis*-[Sm(HL)(DMA)<sub>2</sub>]**·**CH<sub>2</sub>Cl<sub>2</sub> in air gave *trans*-[Sm(HL)(DMA)<sub>2</sub>]**·**CH<sub>2</sub>Cl<sub>2</sub>-ad and *cis*-[Sm(HL)(DMA)<sub>2</sub>]**·**CH<sub>2</sub>Cl<sub>2</sub>-ad, respectively. The PXRD profiles of both air-dried samples were similar in terms of peak positions and only show small differences in relative intensities (Figure S13d, Supporting Information). Air drying leads to loss of volatile CH<sub>2</sub>Cl<sub>2</sub>, which changes the framework structure as shown in the PXRD profiles (see Figures 6 and S13c and d, Supporting Information). The major changes in the PXRD profiles due to air drying are the increased intensity of the peak at 6.75° and the marked decrease in intensity of the peak at 6° to form a vestigial peak (see Figure S13d, Supporting Information). The latter peak is present in the simulated profile for the single crystal structure of *trans*-[Sm(HL)(DMA)<sub>2</sub>]**·**2.8 CH<sub>2</sub>Cl<sub>2</sub>(173 K) (Figure S13d, Supporting Information), while the former is indicative of an intermediated framework structure. The PXRD profiles of both air-dried samples do not have peaks at 7.4° observed for the *cis*-[Sm(HL)(DMA)<sub>2</sub>] framework (Figure 6). Furthermore, strong PXRD peaks observed at 13.26° in *cis*-[Sm(HL)(DMA)<sub>2</sub>] and 11.45° and 12.48° in *trans*-[Sm(HL)(DMA)<sub>2</sub>] framework structures were absent from the PXRD profiles of both *cis*- and *trans*-[Sm(HL)(DMA)<sub>2</sub>]**·**CH<sub>2</sub>Cl<sub>2</sub>-ad (Figures 6 and S12d, Supporting Information). It is evident that the CH<sub>2</sub>Cl<sub>2</sub> exchange framework structure after air drying is independent of the initial [Sm(HL)(DMA)<sub>2</sub>] framework structure and that the *cis* and *trans* framework structures are not present in significant amounts.

The CHCl<sub>3</sub> and C<sub>2</sub>H<sub>4</sub>Cl<sub>2</sub> exchanged *cis*-[Sm(HL)(DMA)<sub>2</sub>] air-dried samples were also studied as well as CH<sub>2</sub>Cl<sub>2</sub>. These solvents are volatile (dichloromethane (B. Pt. = 312.8 K), chloroform (B. Pt. = 334.3 K), and 1,2-dichloroethane (B. Pt. = 357 K)) and have different sizes/shapes. However, the PXRD profiles for *cis*-[Sm(HL)(DMA)<sub>2</sub>]**·**CH<sub>2</sub>Cl<sub>2</sub>-ad, *cis*-[Sm(HL)(DMA)<sub>2</sub>]**·**CHCl<sub>3</sub>-ad, and *cis*-[Sm(HL)(DMA)<sub>2</sub>]**·**C<sub>2</sub>H<sub>4</sub>Cl<sub>2</sub>-ad were very similar (Figures S13b, d and e, Supporting Information). The results above suggest that loss of volatile solvent has led to a stable intermediate phase with only vestigial peaks assignable to the *trans*-[Sm(HL)(DMA)<sub>2</sub>] framework.

The stable intermediate framework [Sm(HL)(DMA)<sub>2</sub>]**·**CH<sub>2</sub>Cl<sub>2</sub> phase PXRD peak at 6.75° is different from the intermediate peak observed in the heat treatment of *trans*-[Sm(HL)(DMA)<sub>2</sub>]**·**DMA<sub>2</sub>H<sub>2</sub>O (intermediate peak at 6.5°) (Figures S12a and b, and, S13d and f, Supporting Information).

**3.3. Gas Sorption Properties.** Flexible MOFs may display some intriguing gas and vapor sorption properties including stepwise and selective adsorption, hysteretic desorption and breathing, gate-opening, and shape-memory effects.<sup>34,38,45,48,51,53</sup> Single crystal to single crystal transformations with gating characteristics for adsorption/desorption were related to sorption isotherms for flexible coordination polymers.<sup>45</sup> The gating mechanism involved rotation of pillars and slippage of layers and is therefore different from the *trans*-

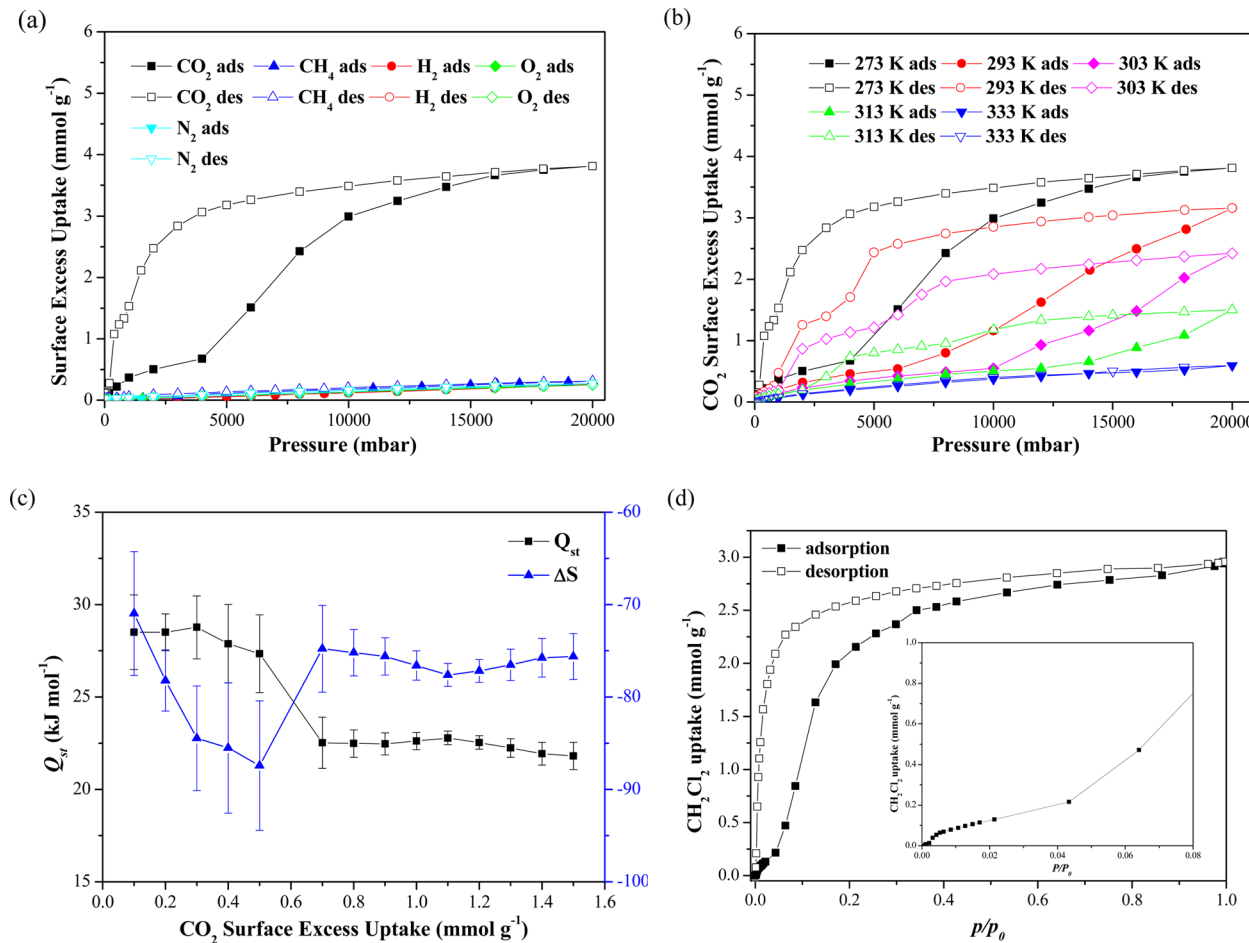


**Figure 7.** Adsorption isotherms for *cis*-[Sm(HL)(DMA)<sub>2</sub>] and variation of CO<sub>2</sub> thermodynamic parameters  $Q_{st}$  and  $\Delta S$  as a function of amount adsorbed. (a) Comparisons of CO<sub>2</sub>, CH<sub>4</sub>, H<sub>2</sub>, N<sub>2</sub>, and O<sub>2</sub> surface excess sorption isotherms at 273 K; (b) CO<sub>2</sub> surface excess sorption isotherms at various temperatures between 273 and 333 K; (c) The isosteric adsorption enthalpies ( $Q_{st}$ ) and entropies ( $\Delta S$ ) of CO<sub>2</sub> for *cis*-[Sm(HL)(DMA)<sub>2</sub>] were calculated from the CO<sub>2</sub> isotherms at low CO<sub>2</sub> surface excess uptakes ( $\leq 0.5 \text{ mmol g}^{-1}$ ) for 273–333 K and for higher CO<sub>2</sub> surface excess uptakes ( $\geq 0.7 \text{ mmol g}^{-1}$ ) for 273–313 K, respectively; (d) CH<sub>2</sub>Cl<sub>2</sub> sorption isotherm at 293 K; the inset shows the isotherm in the low pressure region at the start of gate opening.

[Sm(HL)(DMA)<sub>2</sub>]·DMA·2H<sub>2</sub>O to *cis*-[Sm(HL)(DMA)<sub>2</sub>] gating mechanism. The detailed transport and structure–function relationships for the molecular gating mechanism in the *cis*-[Sm(HL)(DMA)<sub>2</sub>]/*trans*-[Sm(HL)(DMA)<sub>2</sub>] porous system has been investigated by relating structural, thermodynamic, and kinetic aspects in order to bridge the critical gap between the macroscopic data and the transport behavior at the molecular level.

*trans*-[Sm(HL)(DMA)<sub>2</sub>]·DMA·2H<sub>2</sub>O was heat treated at 393 K under ultrahigh vacuum for 4 h to give a fully desolvated (activated) *cis*-[Sm(HL)(DMA)<sub>2</sub>]. High pressure surface excess adsorption isotherms were measured for CO<sub>2</sub>, CH<sub>4</sub>, H<sub>2</sub>, O<sub>2</sub>, and N<sub>2</sub> adsorption on *cis*-[Sm(HL)(DMA)<sub>2</sub>]. Notably, there are only very low surface excess values for CH<sub>4</sub>, H<sub>2</sub>, O<sub>2</sub>, or N<sub>2</sub> by the material at 273 K below 20 bar (Figure 7a).

In contrast to the adsorption isotherms observed for CH<sub>4</sub>, H<sub>2</sub>, O<sub>2</sub>, and N<sub>2</sub>, the adsorption isotherm for CO<sub>2</sub> at 273 K exhibits a gradual step starting at a pressure of ~5 bar with surface excess uptake of ~>0.67 mmol g<sup>-1</sup> (Figure 7a). The maximum CO<sub>2</sub> surface excess capacity for *cis*-[Sm(HL)(DMA)<sub>2</sub>] was 3.81 mmol g<sup>-1</sup> at 273 K and 20 bar ( $p/p_0 = 0.57$ ), equivalent to ~3.2 CO<sub>2</sub> molecules per formula unit (FU).

The desorption isotherm exhibits a broad hysteresis loop, but all of the adsorbed CO<sub>2</sub> was released under vacuum. The presence of the distinct sorption step in *cis*-[Sm(HL)(DMA)<sub>2</sub>] indicates that CO<sub>2</sub> molecules are able to induce a structural transformation to the *trans*-[Sm(HL)(DMA)<sub>2</sub>] framework. The desorption of CO<sub>2</sub> may be influenced by the amine groups that decorate the pore walls in the expanded framework observed in the structure of the “as-synthesized” framework (*trans*-[Sm(HL)(DMA)<sub>2</sub>]·DMA·2H<sub>2</sub>O). However, the  $Q_{st}$  for CO<sub>2</sub> adsorption on *cis*-[Sm(HL)(DMA)<sub>2</sub>] was lower (23–29 kJ mol<sup>-1</sup>) than that observed for direct observation of CO<sub>2</sub> binding for amine functional groups (37–40 kJ mol<sup>-1</sup>) in a functionalized Zn nanoporous MOF.<sup>62</sup>

The CO<sub>2</sub> sorption isotherms were measured at various temperatures to gain insight into the sorption system (Figure 7b). Between 293 and 313 K, the CO<sub>2</sub> adsorption isotherms show the analogous adsorption step with different inflection points corresponding to the different structural transformation onset pressures (Figure 7b). Each structural transformation pressure is lower than the corresponding phase restoration pressure.<sup>34,38,45–47,52</sup> The CO<sub>2</sub> sorption isotherms for the temperature range 273–313 K show that all of the steps take place at approximately the same surface excess of ~0.60 mmol g<sup>-1</sup>, equivalent to ~0.5 CO<sub>2</sub> molecules per FU. Comparison of

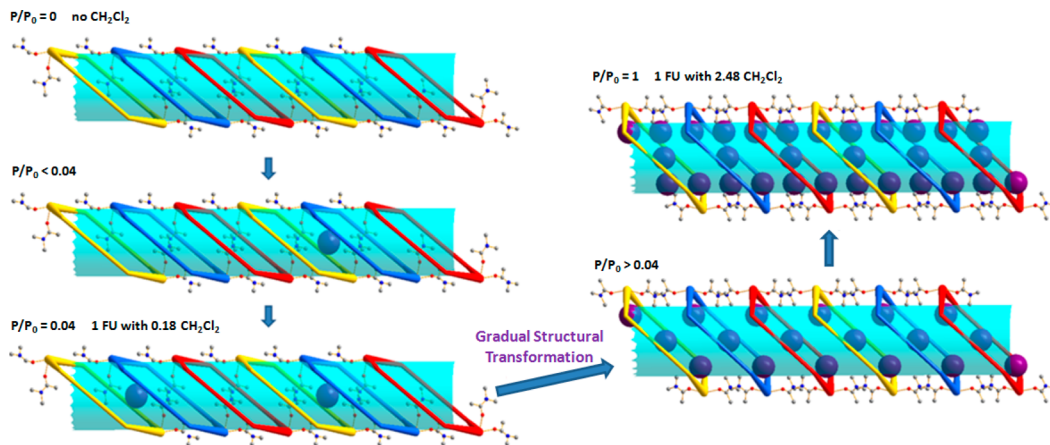


**Figure 8.** Structural transformations of the channel in *cis*-[Sm(HL)(DMA)<sub>2</sub>] induced by CH<sub>2</sub>Cl<sub>2</sub> adsorption. The structural transformation giving the gate-opening behavior and the expansion of framework involves coordinated DMA molecules, which close off the channel by rotating to the *b*-axis. The DMA coordination around the Sm changes from *cis* (O-Sm-O = 76.30°) in *cis*-[Sm(HL)(DMA)<sub>2</sub>] to *trans* (O-Sm-O = 151.21°) in *trans*-[Sm(HL)(DMA)<sub>2</sub>]-DMA·2H<sub>2</sub>O. The resulting framework has greater void volume and therefore is able to accommodate more guest molecules. Three independent networks are shown in red, blue, and yellow. Except for the channel along the *b*-axis and two coordinated DMA molecules, the other sections and atoms of the framework are omitted for clarity.

CO<sub>2</sub> sorption isotherms at 273, 293, and 303 K shows that relative pressures for the appearance of the adsorption step are similar (Figure S17, Supporting Information). These results suggest that the structural transformation is highly dependent on temperature and pressure but occurs at a specific amount of CO<sub>2</sub> adsorbed, which is related to the relative pressure for subcritical adsorption. At 333 K, no apparent adsorption step or major hysteresis was observed in the isotherm (Figure 7b). However, this does not preclude the development of a structural transformation phenomenon at higher (>20 bar) pressures. Similar CO<sub>2</sub> isotherm steps are observed for other materials in the MOF series, for example, *cis*-[Tb(HL)-(DMA)<sub>2</sub>] materials (Figure S19, Supporting Information). The CO<sub>2</sub> sorption isotherm at 273 K gives a maximum surface excess of ~3.81 mmol g<sup>-1</sup> (0.168 g g<sup>-1</sup>) at 20 bar ( $p/p_0 \sim 0.57$ ), and the isotherm is close to reaching a plateau, although some further uptake may occur up to  $p/p_0 = 1$ . This surface excess uptake corresponds to an adsorbed CO<sub>2</sub> volume of 0.162 cm<sup>3</sup> g<sup>-1</sup> assuming a CO<sub>2</sub> density of 1.032 g cm<sup>-3</sup> (CO<sub>2</sub> liquid density at 253 K<sup>63</sup>) and is equivalent to ~77% of the PLATON pore volume of *trans*-[Sm(HL)(DMA)<sub>2</sub>]-DMA·2H<sub>2</sub>O. Small cavities exist between each two adjacent Sm<sup>3+</sup> centers in the framework (Figure 4), which are possibly too small to be accessible for guest molecules but still contribute to the void volume. Accordingly, the framework structure at 273 K and 20 bar pressure in CO<sub>2</sub> atmosphere is very similar to that of the fully open *trans*-[Sm(HL)(DMA)<sub>2</sub>]-DMA·2H<sub>2</sub>O framework structure.

The factors which influence isotherm hysteresis were investigated by measuring two additional CO<sub>2</sub> isotherms at 293 K for 0–1 and 0–5 bar, respectively (Figure S18, Supporting Information). The maximum surface excess uptakes for both isotherms were below the amount (0.6 mmol g<sup>-1</sup> at 6 bar and 293 K), which initiates structural transformation (Figure 7b). A small amount of isotherm hysteresis was observed in both of these isotherms. Thus, the flexible framework of *cis*-[Sm(HL)(DMA)<sub>2</sub>] has minor isotherm hysteresis for the CO<sub>2</sub> isotherms even below the onset of the isotherm step corresponding to the structural framework transformation from *cis* to *trans*-[Sm(HL)(DMA)<sub>2</sub>].

**3.3.1. CO<sub>2</sub> Adsorption Thermodynamics.** The isosteric adsorption enthalpies ( $Q_{st}$ ) and entropies ( $\Delta S$ ) were calculated from the CO<sub>2</sub> isotherms measured at 273–333 K using the isostere (Figures 7c, and S20 and Table S6, Supporting Information). The initial  $Q_{st}$  was ~29 kJ mol<sup>-1</sup> for a surface coverage of 0.1 mmol g<sup>-1</sup>, which is comparable to the previously reported values (25–35 kJ mol<sup>-1</sup>) for porous materials.<sup>6</sup> A gradual decrease was observed before the adsorption isotherm step with  $Q_{st}$  decreasing to ~27 kJ mol<sup>-1</sup> at ~0.5 mmol g<sup>-1</sup>. When the surface coverage increased to 0.7 mmol g<sup>-1</sup>,  $Q_{st}$  decreases abruptly to ~23 kJ mol<sup>-1</sup> and simultaneously  $\Delta S$  increases sharply from ~ -90 to ~ -75 J K<sup>-1</sup> mol<sup>-1</sup>. This is consistent with widening of the pores and increasing disorder. Subsequently,  $Q_{st}$  and  $\Delta S$  are both relatively constant for surface coverage up to 1.5 mmol g<sup>-1</sup>. The significant decrease of  $Q_{st}$  is attributed to the endothermic phase transformation process, which competes with the exothermic adsorption process.<sup>64</sup> The corresponding results shows that  $\Delta S$  increases for the adsorption system (CO<sub>2</sub> – *cis*-[Sm(HL)(DMA)<sub>2</sub>] host) and then maintains a more disordered state due to the continuous phase transformation.<sup>65</sup> Thus, all of the above results are in good agreement with the CO<sub>2</sub>-induced framework transformation from *cis* to *trans*-[Sm(HL)(DMA)<sub>2</sub>].

**3.4. CH<sub>2</sub>Cl<sub>2</sub> Vapor Sorption Properties.** The CH<sub>2</sub>Cl<sub>2</sub> sorption experiments were performed to further explore the unique structural transformation and sorption characteristics (Figure 7d). Similarly, the CH<sub>2</sub>Cl<sub>2</sub> sorption isotherm at 293 K also shows an adsorption step and a broad hysteretic loop. At  $p/p_0 = 0.04$  (CH<sub>2</sub>Cl<sub>2</sub> uptake capacity of ~0.22 mmol g<sup>-1</sup>), the onset of gate opening is shown by the upward isotherm curvature. Differences in the amounts adsorbed to initiate structural transformation may be explained by the difference in molecular volume of CO<sub>2</sub> and CH<sub>2</sub>Cl<sub>2</sub> sorbates. Adsorption increases very steeply for  $p/p_0 = 0.04$  to 0.17. In this relative pressure range, *cis*-[Sm(HL)(DMA)<sub>2</sub>] undergoes a continuous structural framework transformation. The adsorption behavior can be explained by the host–guest and guest–guest interactions and the resulting expansion of the framework and pore volume upon adsorption of CH<sub>2</sub>Cl<sub>2</sub> guest molecules. At  $p/p_0 = 1.00$ , the CH<sub>2</sub>Cl<sub>2</sub> uptake capacity was ~2.95 mmol

$\text{g}^{-1}$ , which corresponds to a total pore volume of  $0.19 \text{ cm}^3 \text{ g}^{-1}$  assuming a  $\text{CH}_2\text{Cl}_2$  density of  $1.33 \text{ g cm}^{-3}$ . This vapor adsorption total pore volume is in agreement with the PLATON pore volume of  $0.19 \text{ cm}^3 \text{ g}^{-1}$  obtained for *trans*-[Sm(HL)(DMA)<sub>2</sub>] $\cdot\text{CH}_2\text{Cl}_2$  (173 K). The PLATON pore volume for *trans*-[Sm(HL)(DMA)<sub>2</sub>] $\cdot\text{DMA}\cdot 2\text{H}_2\text{O}$  was similar ( $0.21 \text{ cm}^3 \text{ g}^{-1}$ ). The structural transformation was reversible with hysteretic adsorption isotherm behavior. The adsorbed  $\text{CH}_2\text{Cl}_2$  molecules were released on reducing the pressure to  $p/p_0 = 0.04$  and completely desorbed under vacuum as shown in the desorption isotherm in Figure 7d.

Combining the results of X-ray analyses and  $\text{CH}_2\text{Cl}_2$  sorption experiments, the results suggest a novel adsorption mechanism in which adsorption induces structural transformations associated with the molecular gate effect (Figure 8) leading to stepwise and hysteretic adsorption. Below  $p/p_0 = 0.04$ , the  $\text{CH}_2\text{Cl}_2$  molecules adsorb without any significant structural change, consistent with the observed isotherm in the low pressure region (Figure 7d inset). The coordinated DMA molecules present in *cis*-[Sm(HL)(DMA)<sub>2</sub>] form a gate for the channel along the *b*-axis. At  $p/p_0 = 0.04$ , the threshold for gate-opening is reached, equivalent to  $\sim 0.2 \text{ CH}_2\text{Cl}_2$  molecules per FU. As the pressure increases further, the structure of the flexible framework begins to transform, coupled with the opening of the pore structure and increased  $\text{CH}_2\text{Cl}_2$  uptake. In this pressure range, the *cis*-[Sm(HL)(DMA)<sub>2</sub>] structure changes, and closed DMA molecular gates progressively rotate to the orientation of the *b*-axis, opening the pore channels. Furthermore, due to expansion of the *cis*-[Sm(HL)(DMA)<sub>2</sub>] framework and increase of available void volume, the  $\text{CH}_2\text{Cl}_2$  uptake capacity ( $\sim 2.5 \text{ CH}_2\text{Cl}_2$  molecules per FU) is close to the saturation uptake capacity of  $\sim 2.8 \text{ CH}_2\text{Cl}_2$  molecules per FU for *trans*-[Sm(HL)(DMA)<sub>2</sub>] $\cdot 2.8\text{CH}_2\text{Cl}_2$  (173 K). The small difference between the theoretical and experimental results can be explained by the presence of small cavities between each two adjacent  $\text{Sm}^{3+}$  centers (Figure 4). Therefore, it is proposed that the material exhibits virtually the same trans framework structure as that of *trans*-[Sm(HL)(DMA)<sub>2</sub>] $\cdot 2.8\text{CH}_2\text{Cl}_2$  (173 K) at  $p/p_0$  close to 1.0 in  $\text{CH}_2\text{Cl}_2$  atmosphere.

**3.5. Adsorption Kinetics for  $\text{CO}_2$ .** **3.5.1. Temperature Swing Kinetics.** Adsorption kinetic profiles for  $\text{CO}_2$  on *cis*-[Sm(HL)(DMA)<sub>2</sub>] were measured at 20 bar for rapid cooling to 273, 293, 303, and 313 K from initial starting conditions of 333 K and 20 bar. The  $\text{CO}_2$  sorption isotherms indicated that the uptake capacity at 333 K and 20 bar was close to that of the threshold for structural transformation. Thus, in order to understand the adsorption kinetics during the structural transformation process, the sample was allowed to reach adsorption equilibrium at a surface excess uptake of  $0.6 \text{ mmol g}^{-1}$  of  $\text{CO}_2$  at 333 K and 20 bar, and this was selected as the initial state prior to structural transformation. The experimental temperature was then changed to 273, 293, 303, and 313 K. The graphs of  $(M_t - M_i)/(M_f - M_i)$  versus time for the adsorption of  $\text{CO}_2$  on *cis*-[Sm(HL)(DMA)<sub>2</sub>] are shown in Figure 9. Here,  $M_t$  is the uptake at time  $t$ ,  $M_f$  is the equilibrium uptake, and  $M_i$  is the initial uptake prior to temperature change. The adsorption kinetics profiles for 273, 293, 303, and 313 K become faster as the change in equilibrium amount increases with decreasing temperature. The time of  $(M_t - M_i)/(M_f - M_i) = 0.5$  ( $t_{1/2}$ ) varies from 293 s for 273 K to 4991 s for 313 K (Table S7, Supporting Information). All of the kinetic profiles were described by a double exponential model (Figure S21, Supporting Information). The final uptakes for the kinetic

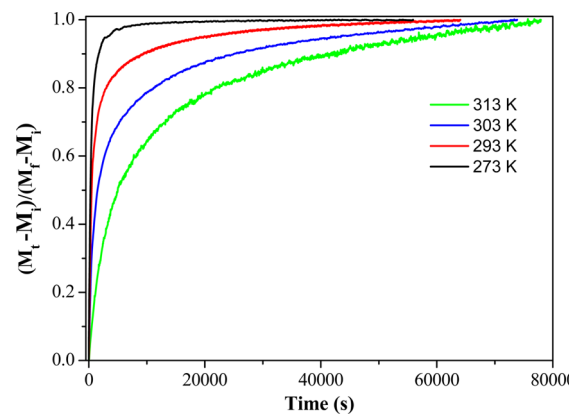


**Figure 9.** Comparison of  $(M_t - M_i)/(M_f - M_i)$  versus time profiles for  $\text{CO}_2$  adsorption on *cis*-[Sm(HL)(DMA)<sub>2</sub>] starting at an initial surface excess uptake of  $0.6 \text{ mmol g}^{-1}$ , 20 bar, and 333 K for temperature change to 273, 293, 303, and 313 K.

profiles are compared with the isotherm uptakes in Table S8 and Figure S22 (Supporting Information). It is evident that the final uptakes from the kinetic profiles are in good agreement with the isotherm uptakes thereby confirming the accuracy of the measurements.

**3.5.2. Isothermal Kinetics.** The  $\text{CO}_2$  isotherm up to 20 bar at 273 K covers the isotherm step for the transition of *cis*-[Sm(HL)(DMA)<sub>2</sub>] to *trans*-[Sm(HL)(DMA)<sub>2</sub>] frameworks and adsorption kinetics were investigated in detail to study the dynamics of the structural change and gating opening process. In the case of porous materials with essentially fixed structures, linear driving force (LDF),<sup>66,67</sup> combined barrier resistance/Fickian diffusion,<sup>68</sup> and Fickian<sup>69</sup> and stretched exponential<sup>70</sup> models have been used to describe diffusion of molecules into these materials. However, the change in the structure of *cis*-[Sm(HL)(DMA)<sub>2</sub>] involving gate opening in response to adsorption makes the description of the diffusion of molecules into *cis*-[Sm(HL)(DMA)<sub>2</sub>] much more complex.

The stretched exponential (SE) kinetic model has been used to describe adsorption kinetics for a wide range of porous materials and does not require any assumptions regarding particle shape/size.<sup>71</sup> The kinetic adsorption/desorption profiles measured in gravimetric studies are for a sample with a particle size distribution and hence represent a distribution of adsorption characteristics. It is very difficult to control the particle size and shape in the synthesis of MOF crystals. This model is described by the following equation:

$$\frac{M_t}{M_e} = 1 - e^{-(kt)^\beta} \quad (2)$$

where  $M_t$  is the mass increase at time  $t$  during the mass relaxation process following the pressure increment,  $M_e$  is the mass increase at equilibrium for pressure increment,  $k$  is the mass transfer rate constant ( $\text{s}^{-1}$ ), and  $t$  is the time (s). The exponent parameter ( $\beta$ ) reflects the width of the distribution of relaxation times and is material dependent. The LDF model<sup>70</sup> is a special case of the SE model when  $\beta = 1$  with a single relaxation time. The process is one-dimensional with a distribution of relaxation times when  $\beta = 0.5$ . All of the kinetic profiles, both prior to and during the isotherm gating step, can be described by this kinetic model (Figures 10a, b, and c, and S23, Supporting Information). It is apparent that values of the kinetic parameter ( $k$ ) are faster and the exponent is smaller,

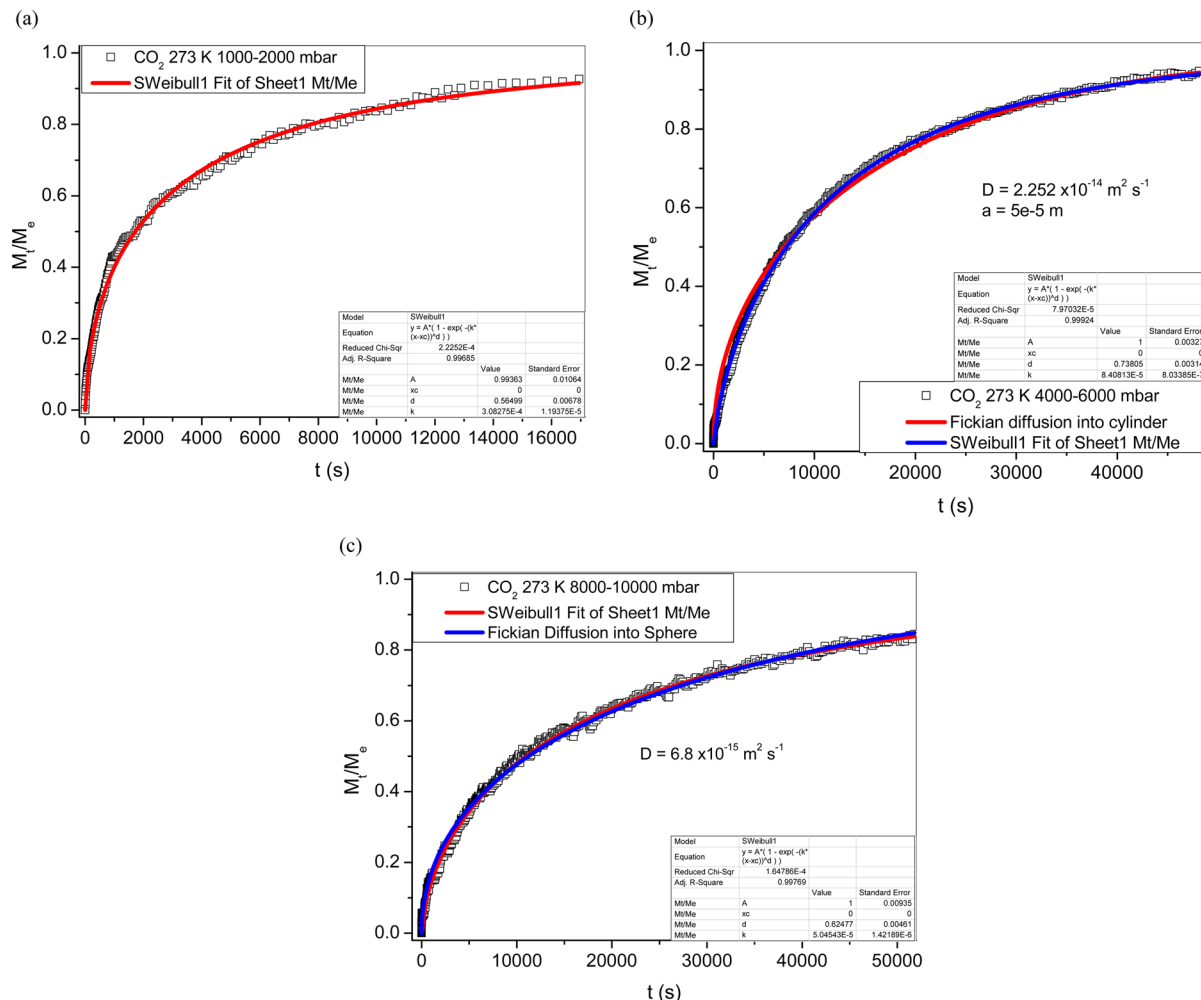


**Figure 10.** Adsorption kinetic profiles for  $\text{CO}_2$  adsorption on *cis*-[Sm(HL)(DMA)<sub>2</sub>] at 273 K for various pressure increments (a) 1000–2000 mbar, (b) 4000–6000 mbar, and (c) 8000–10000 mbar.

prior to the isotherm step. The values for  $\beta$  before the isotherm step are close to that expected for a one-dimensional process.

The SE model also provides good descriptions of Fickian diffusion into porous materials<sup>71</sup> and overlaps with these and related combined barrier resistance/diffusion models (Figure S22, Supporting Information). The stretched exponential function is an approximation for uniformly convergent sums of exponentials.<sup>72</sup> The Fickian diffusion description depends on the shape and size of particles with different equations required for specific particle shapes.<sup>69</sup> An average particle size/dimension has to be used, and this is essentially a scaling factor.

The particles of both *trans*-[Sm(HL)(DMA)<sub>2</sub>]·DMA·2H<sub>2</sub>O and *cis*-[Sm(HL)(DMA)<sub>2</sub>] have needle-like morphology and therefore can be described as approximately cylindrical in shape. Fick's law for isothermal diffusion into a cylindrical particle is given by the equation below:<sup>73</sup>

$$\frac{M_t}{M_e} = 1 - 4 \sum_{n=1}^{\infty} \left( \frac{1}{\zeta_n^2} \right) \exp\left( \frac{-D\zeta_n^2 t}{a^2} \right) \quad (3)$$

where  $D$  is diffusivity ( $\text{m}^2 \text{ s}^{-1}$ ),  $a$  is radius of the cylinder (m), and  $\zeta_n$  the roots of the equation  $J_n(x)$  where  $J_n(x)$  is the Bessel function for zero order and have values of 2.405, 5.520, 8.654, 11.792, 14.931... for  $n = 1, 2, 3, 4, 5...$  etc. The kinetic profile for the 4000–6000 mbar pressure increment can be described by

eq 3. This indicates that diffusion along the pores is the mechanism involved in the dynamics of structural change in response to adsorption. The 6000–8000 and 8000–10000 mbar steps deviate from the above description.

Figure S23 (Supporting Information) shows that the particle shape changes as a result of adsorption of carbon dioxide. Fick's law for isothermal diffusion into a homogeneous spherical particle is given by the equation below:<sup>69</sup>

$$\frac{M_t}{M_e} = 1 - \frac{6}{\pi^2} \sum_{n=1}^{\infty} \left( \frac{1}{n^2} \right) \exp\left( \frac{-Dn^2 \pi^2 t}{r^2} \right) \quad (4)$$

where  $r$  is the particle radius. The kinetic profile for the 8000–10000 mbar pressure increment can be described by eq 4 as shown in Figure 10c. The subtle change in the shape of the kinetic profile is ascribed to particle fragmentation. The 6000–8000 mbar kinetic profile is intermediate between eqs 3 and 4.

The crystals of *cis*-[Sm(HL)(DMA)<sub>2</sub>] and *trans*-[Sm(HL)(DMA)<sub>2</sub>]·DMA·2H<sub>2</sub>O both have needle morphology with the axis of the needle being the C2 *b* crystallographic axis.  $\text{CO}_2$  adsorption results in a change in morphology from needle shaped crystals to irregular shaped particles with more equivalent dimensions, which can be described as approximately spherical shaped particles (Figure S14, Supporting Information). The biggest change in the transition from *cis* to *trans* [Sm(HL)(DMA)<sub>2</sub>] framework is in the *c* crystallographic

axis, which increases from 26.864(18) to 34.21(3) Å (Table S2, Supporting Information). The change in this dimension during adsorption is the most likely cause of the change in particle morphology due to fracturing at faults and dislocations etc. in the crystals. The Fickian diffusion coefficients calculated for pressure increment 4000–6000 mbar and 8000–10000 mbar at 273 K were  $\sim 2.25 \times 10^{-14}$  and  $\sim 6.8 \times 10^{-15} \text{ m}^2 \text{ s}^{-1}$ , respectively. These values are much lower than those obtained for intracrystalline CO<sub>2</sub> diffusion into the metal organic framework ( $8 \times 10^{-13} \text{ m}^2 \text{ s}^{-1}$  at 295 K for IRMOF-1,<sup>74</sup> 1.86  $\times 10^{-12} \text{ m}^2 \text{ s}^{-1}$  at 273 K for CPM-5,<sup>75</sup> and  $7 \times 10^{-13} - 20 \times 10^{-13} \text{ m}^2 \text{ s}^{-1}$  for diffusion along pores NPC-4 at 273 K).<sup>71</sup> This suggests that the structural response of the framework is the rate-determining step in the kinetic process.

**3.6. Selectivity Studies.** Commonly, highly selective hysteretic sorption of CO<sub>2</sub> is found for flexible MOF materials, which have breathing or gate-opening behavior.<sup>53,54,76</sup> In some cases, the initial MOF materials are nonporous without void space to accommodate the guest molecules, while the framework becomes porous by guest-induced structural transformations on increasing the pressure. A partially interpenetrated MOF NOTT-202a showed extremely high single-component gas adsorption selectivity ratios for CO<sub>2</sub> over other small gases, coupled with microscopic CO<sub>2</sub>–host ordering in the micropores below the triple point of CO<sub>2</sub> (216.7 K).<sup>42</sup> At a higher temperature, however, the selectivity in capturing and separating CO<sub>2</sub> from a gaseous mixture declined sharply to  $\sim \text{CO}_2/\text{CH}_4$  of 2.92 at 273 K and 1.41 at 293 K with the disappearance of hysteresis behavior, reflecting a significant limitation in practical applications.

To examine the sorption selectivity and capability of *cis*-[Sm(HL)(DMA)<sub>2</sub>], single-component gas sorption experiments were carried out on CO<sub>2</sub>, CH<sub>4</sub>, H<sub>2</sub>, O<sub>2</sub>, and N<sub>2</sub> at 273 K below 20 bar (Figure 7a). The isotherms have low uptakes with fast kinetics. In contrast, the CO<sub>2</sub> isotherm exhibits a relatively high surface excess capacity of 3.81 mmol g<sup>-1</sup> at 20 bar with stepwise sorption and a broad hysteresis loop. At low pressure, prior to the isotherm step, there is a relatively strong initial interaction between the CO<sub>2</sub> molecules and the host framework as shown by the  $Q_{st} \sim 29 \text{ kJ mol}^{-1}$  at low surface coverage.  $Q_{st}$  decreases rapidly to  $\sim 23 \text{ kJ mol}^{-1}$  as the *cis*-[Sm(HL)(DMA)<sub>2</sub>] framework expands. The large polarizability ( $29.11 \times 10^{25} \text{ cm}^3$ ) and quadrupole moment ( $4.30 \times 10^{26} \text{ esu cm}^2$ ) of CO<sub>2</sub><sup>24,54,77</sup> interacts with the pore surface of *cis*-[Sm(HL)(DMA)<sub>2</sub>] including the amine groups in the linker. The isosteric enthalpy of adsorption is large enough to drive the endothermic structural transformation with an increase in disorder in the system. The selectivity ratio of CO<sub>2</sub> in *cis*-[Sm(HL)(DMA)<sub>2</sub>], obtained from Henry's law, was 6/1, 68/1, 24/1, and 45/1 for CH<sub>4</sub>, H<sub>2</sub>, O<sub>2</sub>, and N<sub>2</sub>, respectively (Tables S10 and 11, and Figures S26 and 27, Supporting Information). Below the isotherm step, at a pressure of 4 bar, the CO<sub>2</sub> isotherm shows type-I characteristics with a plateau in conjunction with gradually decreasing selectivity ratios (Figure S25, Supporting Information). Above this pressure, the *cis*-[Sm(HL)(DMA)<sub>2</sub>] continues adsorbing CO<sub>2</sub> with the highest selectivity ratio of 17/1, 36/1, 22/1, and 22/1 for CO<sub>2</sub>/CH<sub>4</sub>, CO<sub>2</sub>/H<sub>2</sub>, CO<sub>2</sub>/O<sub>2</sub>, and CO<sub>2</sub>/N<sub>2</sub> in this pressure range, respectively (Figure S25, Supporting Information). Intriguingly, remarkable hysteretic desorption is maintained to 4 bar with 20% CO<sub>2</sub> being released, compared with 62%, 82%, 75%, and 69% for CH<sub>4</sub>, H<sub>2</sub>, O<sub>2</sub>, and N<sub>2</sub>, respectively. The selectivity ratios are enhanced by the hysteretic CO<sub>2</sub> desorption coupled with

structural transformation yielding high values at 27/1 for CO<sub>2</sub>/CH<sub>4</sub>, 172/1 for CO<sub>2</sub>/H<sub>2</sub>, 82/1 for CO<sub>2</sub>/O<sub>2</sub>, and 42/1 for CO<sub>2</sub>/N<sub>2</sub> (Table S11, Supporting Information). Additionally, almost all of the trapped gases can be recovered under vacuum, indicating that *cis*-[Sm(HL)(DMA)<sub>2</sub>] can be regenerated without extra activation procedures. Thus, *cis*-[Sm(HL)(DMA)<sub>2</sub>] exhibits high selectivity for CO<sub>2</sub> capture and trapping of CO<sub>2</sub> at ambient temperature. The selectivity at high pressure is enhanced by the framework structural transformation of *cis*-[Sm(HL)(DMA)<sub>2</sub>] to *trans*-[Sm(HL)(DMA)<sub>2</sub>], which gives additional CO<sub>2</sub> capacity, while the other gases (CH<sub>4</sub>, N<sub>2</sub>, etc.) do not transform the *cis*-[Sm(HL)(DMA)<sub>2</sub>] framework structure.

## 4. CONCLUSIONS

The flexible 3-fold interpenetrated *trans*- and *cis*-[Sm(HL)(DMA)<sub>2</sub>] structures exhibit unique and reversible structural transformations upon removal and reintroduction of guest molecules, and an intermediate structural state was also observed in response to adsorption of various chloroalkane (CHCl<sub>3</sub>, C<sub>2</sub>H<sub>4</sub>Cl<sub>2</sub>, and CH<sub>2</sub>Cl<sub>2</sub>) molecules. The “as-synthesized” MOF *trans*-[Sm(HL)(DMA)<sub>2</sub>]·DMA·2H<sub>2</sub>O was fully activated at 393 K under vacuum to give a new single-crystal form *cis*-[Sm(HL)(DMA)<sub>2</sub>]. The activated *cis*-[Sm(HL)(DMA)<sub>2</sub>] material underwent structural transformation during the adsorption of CO<sub>2</sub> and CH<sub>2</sub>Cl<sub>2</sub>. The CO<sub>2</sub> and CH<sub>2</sub>Cl<sub>2</sub> isotherms provide comprehensive experimental evidence for the connection between the structural changes and the observed stepwise and hysteretic sorption features. A detailed characterization of the structures of *trans*-[Sm(HL)(DMA)<sub>2</sub>]·DMA·2H<sub>2</sub>O and *cis*-[Sm(HL)(DMA)<sub>2</sub>] indicate that the mechanism involves coordinated DMA molecules acting as molecular gates by switching from *cis* to *trans* coordination around the Sm to open the framework, thereby providing additional adsorption capacity. The endothermic structural transformation for adsorption of carbon dioxide is driven by the enthalpy of adsorption and entropic effects. Kinetic studies indicate that the mechanism involves CO<sub>2</sub> diffusion along the pores developed as the structural change progresses. The adsorption induced structural transformation of *cis*-[Sm(HL)(DMA)<sub>2</sub>] and hysteretic desorption behavior allows for the capture of CO<sub>2</sub> at high pressure but storage and transport at lower pressure. Adsorption of CH<sub>4</sub>, H<sub>2</sub>, O<sub>2</sub>, and N<sub>2</sub> do not result in the structural transformation of *cis*-[Sm(HL)(DMA)<sub>2</sub>]. This gives rise to exceptional adsorption selectivity of *cis*-[Sm(HL)(DMA)<sub>2</sub>] for CO<sub>2</sub> over other permanent gases (CH<sub>4</sub>, H<sub>2</sub>, O<sub>2</sub>, and N<sub>2</sub>) at high pressure and ambient temperature. The reversible and selective molecular gating characteristics of these frameworks highlight potential sorption applications such as gas separation or molecular recognition.

## ■ ASSOCIATED CONTENT

### S Supporting Information

Details of additional characterization data for the ligands and MOFs in the series; additional crystal structure descriptions and scanning electron micrographs; thermogravimetric analysis; and gas adsorption data including gas adsorption isotherms, isosteric adsorption enthalpy calculation procedures, kinetic data, and equilibrium selectivity information. This material is available free of charge via the Internet at <http://pubs.acs.org>. CCDC 952124–952126 and 1019366 contain the supplementary crystallographic data for this article. These data can be

obtained free of charge from The Cambridge Crystallographic Data Centre via [www.ccdc.cam.ac.uk/](http://www.ccdc.cam.ac.uk/).

## AUTHOR INFORMATION

### Corresponding Authors

<sup>\*</sup>(X.Z.) E-mail: zhaoxuebo@upc.edu.cn.

<sup>\*</sup>(K.M.T) E-mail: mark.thomas@ncl.ac.uk.

### Present Address

<sup>†</sup>School of Chemistry and Chemical Engineering, Qufu Normal University, Qufu, Shandong 273165, P. R. China.

### Notes

The authors declare no competing financial interest.

## ACKNOWLEDGMENTS

We gratefully acknowledge financial support from 'Hundred Talent Project' of CAS (No. KJCX2-YW-W34), and Natural Science Foundation of China (No. 21473256 and No. 21173246) and 'Hemilabile and Switchable Metal–Organic Frameworks' EPSRC award EP/K005499/1.

## REFERENCES

- (1) Eddaoudi, M.; Kim, J.; Rosi, N.; Vodak, D.; Wachter, J.; O'Keeffe, M.; Yaghi, O. M. *Science* **2002**, *295*, 469.
- (2) Zhou, H. C.; Long, J. R.; Yaghi, O. M. *Chem. Rev.* **2012**, *112*, 673.
- (3) Furukawa, H.; Cordova, K. E.; O'Keeffe, M.; Yaghi, O. M. *Science* **2013**, *341*, 974.
- (4) Yaghi, O. M.; O'Keeffe, M.; Ockwig, N. W.; Chae, H. K.; Eddaoudi, M.; Kim, J. *Nature* **2003**, *423*, 705.
- (5) Suh, M. P.; Park, H. J.; Prasad, T. K.; Lim, D. W. *Chem. Rev.* **2012**, *112*, 782.
- (6) Sumida, K.; Rogow, D. L.; Mason, J. A.; McDonald, T. M.; Bloch, E. D.; Herm, Z. R.; Bae, T. H.; Long, J. R. *Chem. Rev.* **2012**, *112*, 724.
- (7) Liu, J.; Thallapally, P. K.; McGrail, B. P.; Brown, D. R. *Chem. Soc. Rev.* **2012**, *41*, 2308.
- (8) Chen, B.; Zhao, X.; Putkham, A.; Hong, K.; Lobkovsky, E. B.; Hurtado, E. J.; Fletcher, A. J.; Thomas, K. M. *J. Am. Chem. Soc.* **2008**, *130*, 6411.
- (9) Li, J. R.; Sculley, J.; Zhou, H. C. *Chem. Rev.* **2012**, *112*, 869.
- (10) Mohideen, M. I. H.; Xiao, B.; Wheatley, P. S.; McKinlay, A. C.; Li, Y.; Slawin, A. M. Z.; Aldous, D. W.; Cessford, N. F.; Duren, T.; Zhao, X.; Gill, R.; Thomas, K. M.; Griffin, J. M.; Ashbrook, S. E.; Morris, R. E. *Nat. Chem.* **2011**, *3*, 304.
- (11) Li, J. R.; Kuppler, R. J.; Zhou, H. C. *Chem. Soc. Rev.* **2009**, *38*, 1477.
- (12) Nugent, P.; Belmabkhout, Y.; Burd, S. D.; Cairns, A. J.; Luebke, R.; Forrest, K.; Pham, T.; Ma, S. Q.; Space, B.; Wojtas, L.; Eddaoudi, M.; Zaworotko, M. J. *Nature* **2013**, *495*, 80.
- (13) Allendorf, M. D.; Bauer, C. A.; Bhakta, R. K.; Houk, R. J. T. *Chem. Soc. Rev.* **2009**, *38*, 1330.
- (14) Cui, Y. J.; Yue, Y. F.; Qian, G. D.; Chen, B. L. *Chem. Rev.* **2012**, *112*, 1126.
- (15) Lee, J.; Farha, O. K.; Roberts, J.; Scheidt, K. A.; Nguyen, S. T.; Hupp, J. T. *Chem. Soc. Rev.* **2009**, *38*, 1450.
- (16) Yoon, M.; Srirambalaji, R.; Kim, K. *Chem. Rev.* **2012**, *112*, 1196.
- (17) Kurmoo, M. *Chem. Soc. Rev.* **2009**, *38*, 1353.
- (18) Horcajada, P.; Chalati, T.; Serre, C.; Gillet, B.; Sebrie, C.; Baati, T.; Eubank, J. F.; Heurtault, D.; Clayette, P.; Kreuz, C.; Chang, J. S.; Hwang, Y. K.; Marsaud, V.; Bories, P. N.; Cynober, L.; Gil, S.; Ferey, G.; Couvreur, P.; Gref, R. *Nat. Mater.* **2010**, *9*, 172.
- (19) Horcajada, P.; Gref, R.; Baati, T.; Allan, P. K.; Maurin, G.; Couvreur, P.; Ferey, G.; Morris, R. E.; Serre, C. *Chem. Rev.* **2012**, *112*, 1232.
- (20) Li, J. R.; Yu, J. M.; Lu, W. G.; Sun, L. B.; Sculley, J.; Balbuena, P. B.; Zhou, H. C. *Nat. Commun.* **2013**, *4*, 1538.
- (21) Xiang, S. C.; He, Y. B.; Zhang, Z. J.; Wu, H.; Zhou, W.; Krishna, R.; Chen, B. L. *Nat. Commun.* **2012**, *3*, 954.
- (22) Maji, T. K.; Matsuda, R.; Kitagawa, S. *Nat. Mater.* **2007**, *6*, 142.
- (23) Deng, H. X.; Doonan, C. J.; Furukawa, H.; Ferreira, R. B.; Towne, J.; Knobler, C. B.; Wang, B.; Yaghi, O. M. *Science* **2010**, *327*, 846.
- (24) Couck, S.; Denayer, J. F. M.; Baron, G. V.; Remy, T.; Gascon, J.; Kapteijn, F. *J. Am. Chem. Soc.* **2009**, *131*, 6326.
- (25) Park, J.; Wang, Z. Y. U.; Sun, L. B.; Chen, Y. P.; Zhou, H. C. *J. Am. Chem. Soc.* **2012**, *134*, 20110.
- (26) Paz, F. A. A.; Klinowski, J.; Vilela, S. M. F.; Tome, J. P. C.; Cavaleiro, J. A. S.; Rocha, J. *Chem. Soc. Rev.* **2012**, *41*, 1088.
- (27) Valtchev, V.; Majano, G.; Mintova, S.; Perez-Ramirez, J. *Chem. Soc. Rev.* **2013**, *42*, 263.
- (28) Cohen, S. M. *Chem. Rev.* **2012**, *112*, 970.
- (29) Horike, S.; Shimomura, S.; Kitagawa, S. *Nat. Chem.* **2009**, *1*, 695.
- (30) Kole, G. K.; Vittal, J. J. *Chem. Soc. Rev.* **2013**, *42*, 1755.
- (31) Xiao, B.; Byrne, P. J.; Wheatley, P. S.; Wragg, D. S.; Zhao, X. B.; Fletcher, A. J.; Thomas, K. M.; Peters, L.; Evans, J. S. O.; Warren, J. E.; Zhou, W. Z.; Morris, R. E. *Nat. Chem.* **2009**, *1*, 289.
- (32) Duan, Z. M.; Zhang, Y.; Zhang, B.; Zhu, D. B. *J. Am. Chem. Soc.* **2009**, *131*, 6934.
- (33) Serre, C.; Mellot-Draznieks, C.; Surble, S.; Audebrand, N.; Filinchuk, Y.; Ferey, G. *Science* **2007**, *315*, 1828.
- (34) Seo, J.; Bonneau, C.; Matsuda, R.; Takata, M.; Kitagawa, S. *J. Am. Chem. Soc.* **2011**, *133*, 9005.
- (35) Chen, B.; Liang, C.; Yang, J.; Contreras, D. S.; Clancy, Y. L.; Lobkovsky, E. B.; Yaghi, O. M.; Dai, S. *Angew. Chem., Int. Ed.* **2006**, *45*, 1390.
- (36) Nelson, A. P.; Farha, O. K.; Mulfort, K. L.; Hupp, J. T. *J. Am. Chem. Soc.* **2009**, *131*, 458.
- (37) Ma, L. Q.; Jin, A.; Xie, Z. G.; Lin, W. B. *Angew. Chem., Int. Ed.* **2009**, *48*, 9905.
- (38) Sakata, Y.; Furukawa, S.; Kondo, M.; Hirai, K.; Horike, N.; Takashima, Y.; Uehara, H.; Louvain, N.; Meilikov, M.; Tsuruoka, T.; Isoda, S.; Kosaka, W.; Sakata, O.; Kitagawa, S. *Science* **2013**, *339*, 193.
- (39) Shekhah, O.; Wang, H.; Paradinas, M.; Ocal, C.; Schupbach, B.; Terfort, A.; Zacher, D.; Fischer, R. A.; Woll, C. *Nat. Mater.* **2009**, *8*, 481.
- (40) Choi, S. B.; Furukawa, H.; Nam, H. J.; Jung, D. Y.; Jhon, Y. H.; Walton, A.; Book, D.; O'Keeffe, M.; Yaghi, O. M.; Kim, J. *Angew. Chem., Int. Ed.* **2012**, *51*, 8791.
- (41) Jiang, H. L.; Makal, T. A.; Zhou, H. C. *Coord. Chem. Rev.* **2013**, *257*, 2232.
- (42) Yang, S. H.; Lin, X.; Lewis, W.; Suyetin, M.; Bichoutskaia, E.; Parker, J. E.; Tang, C. C.; Allan, D. R.; Rizkallah, P. J.; Hubberstey, P.; Champness, N. R.; Thomas, K. M.; Blake, A. J.; Schroder, M. *Nat. Mater.* **2012**, *11*, 710.
- (43) Mulfort, K. L.; Farha, O. K.; Malliakas, C. D.; Kanatzidis, M. G.; Hupp, J. T. *Chem.—Eur. J.* **2010**, *16*, 276.
- (44) Thallapally, P. K.; McGrail, B. P.; Dalgarno, S. J.; Schaef, H. T.; Tian, J.; Atwood, J. L. *Nat. Mater.* **2008**, *7*, 146.
- (45) Seo, J.; Matsuda, R.; Sakamoto, H.; Bonneau, C.; Kitagawa, S. *J. Am. Chem. Soc.* **2009**, *131*, 12792.
- (46) Walton, K. S.; Millward, A. R.; Dubbeldam, D.; Frost, H.; Low, J. J.; Yaghi, O. M.; Snurr, R. Q. *J. Am. Chem. Soc.* **2008**, *130*, 406.
- (47) Thallapally, P. K.; Tian, J.; Kishan, M. R.; Fernandez, C. A.; Dalgarno, S. J.; McGrail, P. B.; Warren, J. E.; Atwood, J. L. *J. Am. Chem. Soc.* **2008**, *130*, 16842.
- (48) Tanaka, D.; Nakagawa, K.; Higuchi, M.; Horike, S.; Kubota, Y.; Kobayashi, L. C.; Takata, M.; Kitagawa, S. *Angew. Chem., Int. Ed.* **2008**, *47*, 3914.
- (49) Cheng, Y.; Kajiro, H.; Noguchi, H.; Kondo, A.; Ohba, T.; Hattori, Y.; Kaneko, K.; Kanoh, H. *Langmuir* **2011**, *27*, 6905.
- (50) Chen, Q.; Chang, Z.; Song, W. C.; Song, H.; Song, H. B.; Hu, T. L.; Bu, X. H. *Angew. Chem., Int. Ed.* **2013**, *52*, 11550.
- (51) Zhao, X.; Xiao, B.; Fletcher, A. J.; Thomas, K. M.; Bradshaw, D.; Rosseinsky, M. J. *Science* **2004**, *306*, 1012.
- (52) Espinal, L.; Wong-Ng, W.; Kaduk, J. A.; Allen, A. J.; Snyder, C. R.; Chiu, C.; Siderius, D. W.; Li, L.; Cockayne, E.; Espinal, A. E.; Suib, S. L. *J. Am. Chem. Soc.* **2012**, *134*, 7944.

- (53) Ferey, G.; Serre, C. *Chem. Soc. Rev.* **2009**, *38*, 1380.
- (54) Choi, H. S.; Suh, M. P. *Angew. Chem., Int. Ed.* **2009**, *48*, 6865.
- (55) Llewellyn, P. L.; Maurin, G.; Devic, T.; Loera-Serna, S.; Rosenbach, N.; Serre, C.; Bourrelly, S.; Horcajada, P.; Filinchuk, Y.; Ferey, G. *J. Am. Chem. Soc.* **2008**, *130*, 12808.
- (56) Stylianou, K. C.; Rabone, J.; Chong, S. Y.; Heck, R.; Armstrong, J.; Wiper, P. V.; Jelfs, K. E.; Zlatogorsky, S.; Bacsa, J.; McLennan, A. G.; Ireland, C. P.; Khimyak, Y. Z.; Thomas, K. M.; Bradshaw, D.; Rosseinsky, M. J. *J. Am. Chem. Soc.* **2012**, *134*, 20466.
- (57) Lin, X.; Jia, J.; Zhao, X.; Thomas, K. M.; Blake, A. J.; Walker, G. S.; Champness, N. R.; Hubberstey, P.; Schroder, M. *Angew. Chem., Int. Ed.* **2006**, *45*, 7358.
- (58) Lin, X.; Telepeni, I.; Blake, A. J.; Dailly, A.; Brown, C. M.; Simmons, J. M.; Zoppi, M.; Walker, G. S.; Thomas, K. M.; Mays, T. J.; Hubberstey, P.; Champness, N. R.; Schroder, M. *J. Am. Chem. Soc.* **2009**, *131*, 2159.
- (59) Lange's *Handbook of Chemistry*, 15th ed.; McGraw-Hill: New York, 1999.
- (60) Spek, A. L. *J. Appl. Crystallogr.* **2003**, *36*, 7.
- (61) Chandler, B. D.; Enright, G. D.; Udachin, K. A.; Pawsey, S.; Ripmeester, J. A.; Cramb, D. T.; Shimizu, G. K. H. *Nat. Mater.* **2008**, *7*, 229.
- (62) Vaidhyanathan, R.; Iremonger, S. S.; Shimizu, G. K. H.; Boyd, P. G.; Alavi, S.; Woo, T. K. *Science* **2010**, *330*, 650.
- (63) *Handbook of Compressed Gases*, 3rd ed.; Van Nostrand Reinhold: New York, 1990.
- (64) Bourrelly, S.; Llewellyn, P. L.; Serre, C.; Millange, F.; Loiseau, T.; Ferey, G. *J. Am. Chem. Soc.* **2005**, *127* (39), 13519.
- (65) Yang, S. H.; Liu, L. F.; Sun, J. L.; Thomas, K. M.; Davies, A. J.; George, M. W.; Blake, A. J.; Hill, A. H.; Fitch, A. N.; Tang, C. C.; Schroder, M. *J. Am. Chem. Soc.* **2013**, *135*, 4954.
- (66) Glueckauf, E.; Coates, J. I. *J. Chem. Soc.* **1947**, 1315.
- (67) Glueckauf, E. *Trans. Faraday Soc.* **1955**, *51*, 1540.
- (68) Loughlin, K. F.; Hassan, M. M.; Fatehi, A. I.; Zahur, M. *Gas Sep. Purif.* **1993**, *7*, 264.
- (69) Crank, J. *The Mathematics of Diffusion*, 2nd ed.; Clarendon Press: Oxford, U.K., 1975.
- (70) Klafter, J.; Shlesinger, M. F. *Proc. Natl. Acad. Sci. U.S.A.* **1986**, *83*, 848.
- (71) Li, L. J.; Bell, J. G.; Tang, S. F.; Lv, X. X.; Wang, C.; Xing, Y. L.; Zhao, X. B.; Thomas, K. M. *Chem. Mater.* **2014**, *26*, 4679.
- (72) Anderssen, R. S.; Edwards, M. P.; Husain, S. A.; Loy, R. J. *19th International Congress on Modelling and Simulation (Modsim2011)*; The Modelling and Simulation Society of Australia and New Zealand Inc.; 2011; p 263.
- (73) Anderson, R. B.; Bayer, J.; Hofer, L. J. E. *Ind. Eng. Chem. Process Des. Dev.* **1965**, *4*, 167.
- (74) Zhao, Z. X.; Li, Z.; Lin, Y. S. *Ind. Eng. Chem. Res.* **2009**, *48*, 10015.
- (75) Sabouni, R.; Kazemian, H.; Rohani, S. *Microporous Mesoporous Mater.* **2013**, *175*, 85.
- (76) Wu, H. H.; Reali, R. S.; Smith, D. A.; Trachtenberg, M. C.; Li, J. *Chem.—Eur. J.* **2010**, *16*, 13951.
- (77) Llewellyn, P. L.; Bourrelly, S.; Serre, C.; Filinchuk, Y.; Ferey, G. *Angew. Chem., Int. Ed.* **2006**, *45*, 7751.